Petrogenesis and geodynamic implications of two episodes of Permian and Triassic high-silica granitoids in the Chinese Altai, Central Asian Orogenic Belt

Article · August 2019

DOI: 10.1016/j.jseaes.2019.103978

8 authors, including:

Zhengfan Lin
Chinese Academy of Sciences
5 PUBLICATIONS **11** CITATIONS
SEE PROFILE

Chao Yuan
Chinese Academy of Sciences
386 PUBLICATIONS **9,808** CITATIONS
SEE PROFILE

Yunying Zhang
The University of Hong Kong
30 PUBLICATIONS **248** CITATIONS
SEE PROFILE

Min Sun
The University of Hong Kong
301 PUBLICATIONS **24,693** CITATIONS
SEE PROFILE

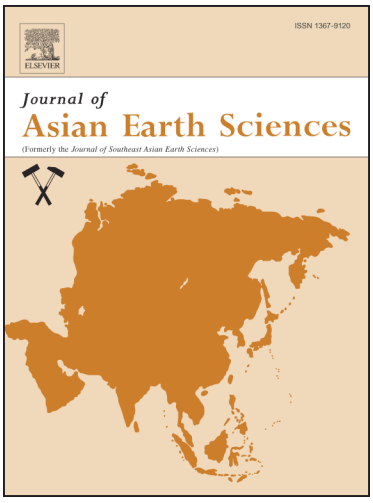

Petrogenesis and geodynamic implications of two episodes of Permian and Triassic high-silica granitoids in the Chinese Altai, Central Asian Orogenic Belt

Zhengfan Lin, Chao Yuan, Yunying Zhang, Min Sun, Xiaoping Long, Xinyu Wang, Zongying Huang, Zhiwei Chen

PII: S1367-9120(19)30330-X
DOI: https://doi.org/10.1016/j.jseaes.2019.103978
Reference: JAES 103978

To appear in: *Journal of Asian Earth Sciences*

Received Date: 5 June 2019
Revised Date: 18 August 2019
Accepted Date: 20 August 2019

Please cite this article as: Lin, Z., Yuan, C., Zhang, Y., Sun, M., Long, X., Wang, X., Huang, Z., Chen, Z., Petrogenesis and geodynamic implications of two episodes of Permian and Triassic high-silica granitoids in the Chinese Altai, Central Asian Orogenic Belt, *Journal of Asian Earth Sciences* (2019), doi: https://doi.org/10.1016/j.jseaes.2019.103978

Petrogenesis and geodynamic implications of two episodes of Permian and Triassic high-silica granitoids in the Chinese Altai, Central Asian Orogenic Belt

Zhengfan Lin[a,b,c], Chao Yuan[a,*], Yunying Zhang[a,c], Min Sun[c], Xiaoping Long[d], Xinyu Wang[a], Zongying Huang[a], Zhiwei Chen[a,b]

[a]State Key Laboratory of Isotope Geochemistry, Guangzhou Institute of Geochemistry, Chinese Academy of Sciences, Guangzhou 510640, China

[b]University of Chinese Academy of Sciences, Beijing 10069, China

[c]Department of Earth Sciences, The University of Hong Kong, Pokfulam Road, Hong Kong

[d]State Key Lab of Continental Dynamics, Department of Geology, Northwest University, Northern Taibai Street 229, Xian 710069, China

[*]Corresponding author. Tel.: +86 20 85290708; fax: +86 20 85290130.
E–mail address: yuanchao@gig.ac.cn (C. Yuan).

Abstract

Tectonic transition from post-collision to intraplate settings is a crucial process in orogenic belts. To characterize such a transition in the Chinese Altai, we conduct an integrated study on Permian to Triassic granitoids. Zircon U–Pb dating reveals that the granitoids can be subdivided into two stages: early Permian (291–286 Ma) and late

Triassic (216–209 Ma). Granitoids of both two stages exhibit high SiO_2, low Mg#, low Cr and Ni contents, and variable Sr–Nd–Hf isotopes, all of which indicate a multiple crustal origin. Generally, the Triassic granitoids have similar εNd(t) but relatively higher εHf(t) values than those of the Permian granitoids. Moreover, the Triassic granitoids possess relatively higher ASI and more variable Al_2O_3/TiO_2, CaO/Na_2O, Rb/Sr and Rb/Ba values than those of the Permian granitoids, suggesting that the Triassic magmatic sources were much variable and complicated with higher proportions of sediments. By integrating regional data, two magmatic peaks at Permian and Triassic can also be recognized. From early Permian to Triassic, the SiO_2, $Na_2O + K_2O$ and Th contents, ASI and $^{87}Sr/^{86}Sr$, Al_2O_3/TiO_2, Rb/Sr and Rb/Ba values for the felsic rocks gradually increase, implying more and more strongly reworking of continental crust. Also, the Rb, Y + Nb and Yb + Ta concentrations for felsic rocks progressively increase from early Permian to Triassic, demonstrating a geodynamic evolution from syn/post-collision to intraplate settings. Furthermore, we propose that the post-collision and intraplate tectonism, especially the latter, could facilitate the generation of high-silica granites, which drive maturation of continental crust in accretionary orogenic belts.

Keywords: Chinese Altai; Post-collision; Intraplate; High-silica granitoids

1. Introduction

The tectonic transition from a post-collision to an intraplate environment

accompanied by changes in deformation, metamorphism and magmatism is a basic process in orogenic belts (Black and Liegeois, 1993; Liegeois et al., 1998; Bonin et al., 1998; Bonin, 2004; Tadayon et al., 2017). Generally, high-temperature low-pressure metamorphism may occur during the post-collision extension stage (Gerdes et al., 2000; Janoušek and Holub, 2007), while strike-slip or transtensional shear zones can be activated during the intraplate period (Nikishin et al., 2002; Duggen et al., 2005). In addition, these two tectonic settings are characterized by contrasting magmatic types and associations, such as I- and A2-type granitoids for post-collisional settings, and S- and A1-type granitoids for intraplate settings (Eby, 1992; Sylvester, 1998; Bonin, 2007). However, the records of post-collision metamorphism and deformation are usually obscured by later intraplate tectonic events in ancient orogenic belts (Willner et al., 2009). In this case, investigating the geochemical changes in magmatism may provide crucial insights into the tectonic transition from post-collision to intraplate settings.

High-silica (SiO_2 > 70 wt.%) granites (HSG) or their volcanic counterparts are products of repeated melting of existing crustal materials, which usually take place under the post-collision or intraplate settings (Bonin et al., 1998; Glazner et al., 2008; Lee and Morton, 2015). Granitoids of such kind are important carriers of highly incompatible elements (Wu et al., 2017). Since re-melting of HSGs will produce felsic melts geochemically similar to their source materials, the widespread occurrence of high-silica granitic rocks is a key feature of highly evolved and geochemically stable continental crust (Rudnick and Gao, 2003; Wu et al., 2017). Therefore, studying the HSGs can provide crucial constraints on the evolution of the continental crust,

especially the geochemical differentiation between upper and middle–lower continental crust (Glazner et al., 2008; Bachmann and Bergantz, 2008; Lee and Morton, 2015).

The Chinese Altai is located on the southwestern margin of the Central Asian Orogenic Belt (CAOB, Fig. 1a) (Sengör et al., 1993; Sengör and Natal'in, 1996; Jahn et al., 2000; Zhang et al., 2018), flanked by the Sayan and Gorny Altai in the north and the Junggar Block in the south. It was formed as a Paleozoic accretionary complex accompanied by intrusion of voluminous arc magmas, and was docked with the Junggar Block during the late Paleozoic (Yuan et al., 2007a, 2007b; Cai et al., 2011; Tong et al., 2014a). The Chinese Altai is marked by voluminous granites and gneissic granitoids occupying ca. 70% of its surface area (Windley et al., 2002). As one important type of granitoids in the Chinese Altai, the HSGs are widely developed during the early Permian and late Triassic periods, which possibly correspond to the post-collision and intraplate stages, respectively (Windley et al., 2002; Wang et al., 2007, 2009, 2010). Though some studies have been conducted on these granitoids, little attention was paid to the difference between these two episodes of igneous activities. Neither did previous studies discuss the high-silica nature of such granitic magmatism and their implications for the maturation of the continental crust in the Chinese Altai. In this contribution, we conduct integrated geochronological, whole-rock geochemical and Sr–Nd–Hf isotopic analyses on six high-silica granitic plutons formed in the Permian and Triassic in the Chinese Altai. These newly obtained data together with previously reported data can shed new lights on the above issues.

2. Geological background and sample description

2.1. Geological background

The Chinese Altai is separated from the Junggar Block to the south by the Erqis Fault, which is one of the largest strike-slip fault systems in Asia and an important structural element within the CAOB extending for over 1000 km in length (Sengör et al., 1993; Buslov et al., 2004; Fig. 1a and b). The Chinese Altai has received much attention from the geology community for its accretionary orogenesis, prominent crustal growth and abundance of mineral resources (Sengör and Natal'in, 1996; Windley et al., 2002; Xiao et al., 2004; Wang et al., 2009, 2010). It experienced a long-lasting subduction process throughout the Paleozoic, and the majority of the sedimentary records reflect a fore-arc setting (Windley et al., 2002; Xiao et al., 2004). Tectonically, the Chinese Altai are segmented into several NW–SE trending units with distinct sedimentary and magmatic features bounded by a series of subparallel faults. A six-unit segmentation scheme from Windley et al. (2002) is presented in Figure 1b, in which Units 1–5 are located north of the Erqis Fault while Unit 6 is on the south of the Erqis fault as a part of the Junggar Block.

Sedimentary rocks in northern Chinese Altai, especially Units 1–3, are dominated by a group of thick metagreywackes known as the Habahe Group, which has been considered to be deposited during the middle Ordovician based on recent detrital zircon data (Long et al., 2007). The early Paleozoic zircons in the Habahe Group have a wide range of Hf isotopic compositions with $\varepsilon Hf(t)$ values from –20 to +15, but positive values account for the majority (Long et al., 2007; Sun et al., 2008; Wang et al., 2011).

On the other hand, whole-rock Sr–Nd isotopic measurements present relatively enriched compositions with initial $^{87}Sr/^{86}Sr$ being 0.7109 to 0.7131 and εNd(t) being –5.2 to –4.2 (Liu et al., 2012). In southern Chinese Altai, especially Unit 4, the late Silurian to early Devonian Kangbutiebao Formation and late Devonian Altai Formation are widely exposed (Windley et al., 2002; Chai et al., 2009). The Kangbutiebao Formation comprises arc-related volcanic and pyroclastic rocks (Windley et al., 2002; Xiao et al., 2004), with Sr–Nd isotopic compositions ($(^{87}Sr/^{86}Sr)_i$ = 0.7062–0.7094; εNd(t) = –2.9 to +0.1) more depleted than those of the Habahe Group (Liu et al., 2012). The Altai Formation, which consists mainly of tuffaceous turbidites interlayered with Mg-rich dacite, unconformably rests on the Kangbutiebao Formation (Windley et al., 2002). It has enriched Sr–Nd isotopic compositions ($(^{87}Sr/^{86}Sr)_i$ = 0.7106–0.7117; εNd(t) = –6.0 to –5.5), which are similar to those of the Habahe Group (Liu et al., 2012).

Granitic magmatism is widely developed in the Chinese Altai, with multiple episodes. The early to middle Paleozoic granitoids spread across the whole Chinese Altai, and are dominated by I-type granites (Wang et al., 2009, 2010). In contrast, the early Permian and late Triassic granitoids are commonly found in the southern Chinese Altai. The former are featured by associations of I- and A-type granites with εNd(t) from –5 to +10 and εHf(t) from 0 to +10, while the latter are typically associations of I- and S-type granites and display more enriched Nd isotopic compositions with εNd(t) below 0 but similar εHf(t) compared to the former (Wang et al., 2009; Yu et al., 2017a, 2017b).

2.2. Sample description

Thirty-nine samples were collected from six granitic intrusions from the Chinese Altai in this study, and their locations are shown on Figure 1b.

The Fuyun granitic dyke is located ca. 10 km southwest of the Fuyun city. It extends in the NNW–SSE direction, in perpendicular to the regional faults. The sample is fine- to intermediate-grained with feldspar and quartz typically 1–2 mm in size, and displays a hypidiomorphic granular texture (Fig. 2a). It consists of quartz (35 vol.%), orthoclase (25 vol.%), plagioclase (35 vol.%) and minor amounts of biotite.

The Kalasu biotite granite and Halasu two-mica granite are located near the center of the Chinese Altai and ca. 7.5 km northwest of the Altay city. Both of them are fine-grained with grain sizes typically in a range of 0.5–1.0 mm (Fig. 2b and c). The Kalasu biotite granite is composed of quartz (35 vol.%), orthoclase (20 vol.%), plagioclase (40 vol.%) and biotite (5 vol.%), while the Halasu dual-mica granite consists of quartz (35 vol.%), orthoclase (30 vol.%), plagioclase (30 vol.%) and muscovite (5 vol.%). The biotite and muscovite grains are euhedral.

The Xibuodu biotite granite is located in the south of the Chinese Altai and ca. 45 km east of the Fuyun city. The outcrop is in an oval shape with 5 km in length. It mostly contains quartz (35 vol.%), orthoclase (20 vol.%), plagioclase (40 vol.%) and biotite (5 vol.%). It has a coarse-grained texture with grain sizes typically in the range of 3–6 mm (Fig. 2d).

The Shangkelan albite-rich granite is a small pluton located ca. 15 km of the northeast of the Altay city. Pegmatitic veins are developed within this pluton, some of

which host Nb–Ta mineralization (Chen et al., 2002). Rocks of the Shangkelan albite-rich granite show a coarse-grained texture (Fig. 2e), and are comprised of plagioclase (25 vol.%), alkali feldspar (35 vol.%), quartz (30 vol.%), biotite (5%) and muscovite (5%). The plagioclase and quartz grains are usually larger than 1 cm.

The Alaer biotite granite is located near the northeastern border of the Chinese Altai, ca. 35 km northeast of the Fuyun city. Samples of this granite show a coarse-grained porphyritic texture (Fig. 2f). The phenocrysts (40 vol.%) consist of microcline up to 5 cm in length. The groundmass comprises euhedral biotite (5 vol.% of groundmass, same below), semi-euhedral orthoclase (25 vol.%), plagioclase (40 vol.%) and quartz (30 vol.%).

3. Analytical methods

Fresh rock samples selected for zircon U–Pb dating were cut into small chips with an electric cutter and examined to avoid any weathered surfaces or veins. The fresh chips were ground down to 80 mesh size in a steel ball mill, then separated for zircons by heavy-liquid and magnetic techniques and further purified by handpicking under a binocular microscope to avoid visible cracks or inclusions. The selected grains were mounted on an epoxy resin disk and polished to about half of their thickness in order to expose their internal structure. Cathodoluminescence (CL) images were acquired with a Mono L3 CL imaging system mounted on a JEOL JXA–8100 EPMA, at the State Key Laboratory of Isotope Geochemistry, Guangzhou Institute of Geochemistry, Chinese Academy of Sciences (SKLIG GIG CAS). The CL images were used in addition to

reflective and transmissive light photographs to assist the selection of analytical positions.

Zircon U–Pb dating was carried out with a RESOlution M-50/Agilent 7500a LA–ICP–MS system at the SKLIG GIG CAS. The U–Pb isotope fractionation effect was corrected using 91500 zircon standard. Common lead was corrected following the approach of Andersen (2002). The 91500 and NIST SRM 610 zircon standards were measured after every 10 samples for drift correction and quality control. The U–Pb data processing and plotting were performed by using the ICPMSDataCal 8.0 (Lin et al., 2016) and IsoPlot 3.5 (Ludwig et al., 2003).

Fresh rock samples selected for geochemical analyses were cut into blocks approximately 5 cm in size with an electric cutter. Those blocks were crushed and cleaned with deionized water and then ground to around 200 mesh size. The whole-rock major oxides were measured by a Rigaku ZSX100e X-ray fluorescence spectrometry (XRF), with powdered samples fused into $Li_2B_4O_7$-based glass disks after loss-of-ignition measurements. Trace element compositions were analyzed by a Perkin-Elmer Sciex ELAN 6000 ICP–MS with acid-dissolved samples. Both analyses were conducted at the SKLIG GIG CAS. Analytical uncertainties for both major oxides and trace elements vary within 1–5%. Quality control of XRF data uses a set of internally developed standards while trace element data make use of international standard materials including BHVO-2 and AGV-2 and national standards including GSR-1, GSR-2 and GSR-3. Detailed description of the analytical procedures used is given in Li et al. (2006).

Whole-rock Sr–Nd–Hf isotopic compositions were analyzed using a Neptune Plus Multi–Collector ICP–MS at the SKLIG GIG CAS, with acid-dissolved samples. Elemental separation was performed using varied resin columns. Sr and REEs were separated using DGA Spec resin column, followed by REE separation using HDEHP-coated KEF columns to obtain Nd. Hf was separated and purified using LN resin. During analysis, measured values for the NBS987 Sr standard, JNdi-1 Nd standard and JMC-14374 Hf standard were 0.710248 ± 63 for $^{87}Sr/^{86}Sr$, 0.512115 ± 22 for $^{143}Nd/^{144}Nd$, and 0.282186 ± 24 for $^{176}Hf/^{177}Hf$, respectively (errors are 2σ). The detailed analytical procedures are similar to those in Wei et al. (2002) and Li et al. (2006).

4. Analytical results

The U–Pb isotopic data for the granitoid samples from the Chinese Altai are presented in Table S1 (supplementary materials). Analytical results of whole-rock major oxides, trace elements and Sr–Nd–Hf isotopes are listed in Tables 2–4, respectively. Whole-rock major and trace element data from Tong (2006) for the Halasu Granite and major element data from Tong et al. (2014a) for the Shangkelan Granite were also used in the following discussion.

4.1. Zircon geochronology

Sample FY-0 from the SW-Fuyun granitic dyke was selected for zircon U–Pb dating, and the zircons from this sample are transparent and euhedral with sizes of 50

to 100 μm in length and aspect ratios from 1 to 2. Twenty-five representative zircons with clear concentric oscillatory zoning were analyzed and yielded high Th/U ratios (0.1–1.1). Eleven among the analyzed grains gave concordant U–Pb ages, and seven form a population with $^{206}Pb/^{238}U$ ages ranging between 282 Ma and 298 Ma, which yielded a weighted mean age of 291.4 ± 5.5 Ma (Fig. 3a). The remaining four zircons obtained relatively old ages (324–417 Ma), which probably represent ages of inherited zircons.

Sample KLS-0 from the Kalasu granite was chosen for zircon U–Pb dating. The zircons from this sample are transparent and mostly euhedral, and are 50–150 μm long and have aspect ratios of 1–4. All of the zircon grains developed fine oscillatory rings, typical feature of igneous zircon. Twenty-two zircon grains were analyzed, and fifteen grains gave concordant U–Pb ages with high Th/U ratios (0.2–1.1). Among them, twelve zircon points yielded a weighted mean $^{206}Pb/^{238}U$ age of 286.6 ± 4.0 Ma (Fig. 3b), representing the crystallization age of the Kalasu granite, while the other three concordant points gave relatively old ages (342–443 Ma), possibly representing inherited zircons from the source.

Sample HLS-0 from the Halasu granite was selected for zircon U–Pb isotopic analysis. The zircons are transparent and euhedral, and have lengths of 50–100 μm with aspect ratios of 1–3. Most grains show clear oscillatory rings, consistent with an igneous origin, and twenty-seven zircons were analyzed. Only fifteen analyses gave concordant U–Pb ages with Th/U ratios of 0.33–0.90, and six of them from 278 to 302 Ma cluster a population, yielding a weighted mean $^{206}Pb/^{238}U$ age of 285.9 ± 11 Ma (Fig. 3c). In

addition, six analyses gave relatively old ages (402–535 Ma), possibly showing inheritance of the magma source. The remaining three analyses have apparent ages in the range of 92–222 Ma. These three zircons are characterized by anomalously high uranium contents (1121–14314 ppm) and show relatively dark CL images. Zircons with high U contents (> 1000 ppm) may experience significant radiation damage, and thus may no longer preserve closeness for U and Pb, resulting in interruptions to their U–Pb clocks (Ewing et al., 2003). Therefore, these three young ages may not record the formation ages and thus were not used in the calculation.

Twenty-eight zircon grains from the Alaer biotite granite (sample ALR-0) were analyzed for U–Pb dating. The zircons are transparent and euhedral, and have lengths of 100–250 μm with aspect ratios of 1–5. On CL images, most of the zircons display clear oscillatory rings, typical of igneous origin. Fourteen ablation points from this sample yielded concordant $^{206}Pb/^{238}U$ ages from 209 Ma to 287 Ma and Th/U ratios within 0.2–1.5. A cluster of eleven ablation points yielded a weighted mean $^{206}Pb/^{238}U$ age of 216.3 ± 3.1 Ma (Fig. 3d), which is interpreted to represent the emplacement age of the Alaer granite. This age is in close agreement with data acquired by Liu et al. (2014). The remaining three concordant analyses yielded old ages from 241 to 287 Ma.

Sample XBD-0 from the Xibuodu biotite granite was chosen for zircon U–Pb dating, zircons from this sample are mostly transparent and euhedral and have lengths from 100 to 200 μm with length/width ratios within 1–4. The zircons display clear oscillatory zoning, suggesting a magmatic origin. Twenty among the twenty-nine analyses yielded concordant $^{206}Pb/^{238}U$ ages and high Th/U ratios between 0.15 to 1.29.

Among the twenty concordant ages, fourteen form a population and yielded a weighted mean $^{206}Pb/^{238}U$ age of 212.9 ± 4.2 Ma (Fig. 3e), which is interpreted to represent the crystallization age of the Xibuodu granite, while the other six gave old ages of 242–272 Ma, possibly showing inheritance of the magma source.

Twenty-three zircon grains from the Shangkelan biotite granite (sample SKL-0) were analyzed for U–Pb dating. The zircons are euhedral and have lengths of 50–150 μm and length/width ratios between 1 and 6. On CL images, the grains display clear oscillatory rings, typical of igneous origin. Fourteen ablation points for this sample yielded Th/U ratios of 0.15–1.02 and concordant $^{206}Pb/^{238}U$ ages that form two populations. One population of six grains includes U–Pb ages from 234 to 257 Ma, and the other population of eight grains gave a weighted mean $^{206}Pb/^{238}U$ age of 209.2 ± 4.1 Ma (Fig. 3f). The latter is interpreted to be the crystallization age of the Shangkelan granite.

Overall, the studied granitic intrusions formed within two stages, one in the early to middle Permian (291–286 Ma) and the other in the late Triassic (216–209 Ma).

4.2. Whole-rock major and trace geochemistry

4.2.1. Permian granitic intrusions

The Permian granitic intrusions (Kalasu, Halasu and SW-Fuyun) of this study are characterized by similar major oxide compositions. Their high SiO_2 (70.3–75.8 wt.% except one sample) and high K_2O (3.5–4.9 wt.%) contents (Fig. 4a and b) are comparable to those of the HSGs described by Lee and Morton (2015) and Wu et al.

(2017). In addition, they have relatively high Na_2O (3.2–4.5 wt.%) but low CaO (0.2–2.0 wt.%), $Fe_2O_3^T$ (1.6–2.9 wt.% except one sample) and MgO (0.09–0.91 wt.%) contents as well as low Mg# (10.2–37.9) (Fig. 4c). Rocks of the Permian granitoids display weakly peraluminous features with aluminum saturation index (ASI) being 1.04–1.22 (Fig. 4d). They belong to the high-K calc-alkaline series based on their high K_2O concentrations (Fig. 4b) and K_2O/Na_2O ratios (0.7–1.3).

The Permian granitic intrusions have variable concentrations of Sr (34.1–179 ppm), Rb (95.4–445 ppm) and Ba (258–673 ppm). Rocks of the SW-Fuyun and Halasu granites possess relatively low Rb/Ba (0.15–0.93) and Rb/Sr (0.54–3.5) ratios, while those of the Kalasu granite possess relatively high Rb/Ba (0.68–0.92) and Rb/Sr (1.6–6.0) ratios. All the three granites have low Ga/Al ratios (10000*Ga/Al = 1.9–3.0) and low Zr + Nb + Ce + Y concentrations (146–369 ppm), and display marked light REE (LREE) enrichment ($(La/Yb)_N$ = 1.9–9.8) and significantly negative Eu anomaly (δEu = 0.25–0.64) (Fig. 5a). Their primitive mantle normalized trace element spider-diagrams show depletion of high field strength elements (HSFE) such as negative Nb, Ta and Ti anomalies, but enrichment of large ion lithophile elements (LILE) such as positive Rb, Th and U anomalies (Fig. 5b).

4.2.2. Triassic granitic intrusions

The Triassic granitic intrusions (Alaer, Xibuodu and Shangkelan) of this study have major oxide compositions similar to those of the Permian counterparts, namely high SiO_2 (71.0–77.2 wt.%) and high Na_2O (2.7–5.5 wt.%), and high but variable K_2O

(1.2–6.8 wt.%) contents (Fig. 4a and b). Rocks from these three plutons are also marked by low $Fe_2O_3^T$ (0.7–3.3 wt.%) and low MgO (0.06–0.67 wt.%) as well as low Mg# (14.1–37.4) (Fig. 4c). Samples of the Triassic Alaer and Xibouodu granites display weakly peraluminous compositions with ASI ratios between 1.02 and 1.19 (Fig. 4d), while Shangkelan is more enriched in Al, with ASI = 1.08–1.45. The three intrusions fall into the fields of calc-alkaline and high-K calc-alkaline series based on their SiO_2–K_2O relationships (Fig. 4b).

The Triassic granitic intrusions possess more variable trace element compositions compared to the Permian counterparts, such as varied Sr (14.3–853 ppm), Rb (95.5–528 ppm) and Ba (20.2–1660 ppm) contents. The Shangkelan granite is characterized by intermediate to high Rb/Ba (2.3–15) and Rb/Sr (2.1–15) ratios, whereas the Alaer and Xibuodu granites have relatively low Rb/Ba (0.13–2.8) and Rb/Sr (0.32–5.9) ratios. Similar to the Permian granites, all of the three Triassic granites possess low Ga/Al ratios (10000*Ga/Al = 1.4–3.1) and low Zr + Nb + Ce + Y contents (43.9–450 ppm), and are featured by significant LREE enrichment ($(La/Yb)_N$ = 1.6–29) and prominently to weakly negative Eu anomalies (δEu = 0.19–0.99 except one sample with δEu = 1.56) (Fig. 5c). On the primitive mantle normalized trace element spider-diagrams (Fig. 5d), the Triassic granitic samples display prominent depletion of Nb and Ta but negligible Zr and Hf anomalies. Relative to the Alaer and Xibuodu granites, the Shangkelan granite shows stronger negative anomalies of Ba, Sr and Ti (Fig. 5d).

4.3. Whole-rock Sr–Nd–Hf isotopic compositions

4.3.1. Permian granitic intrusions

The three Permian granites (SW-Fuyun, Halasu and Kalasu) in this study have different isotopic compositions (Fig. 6a and b). The SW-Fuyun granite is characterized by relatively low $(^{87}Sr/^{86}Sr)_i$ (0.7040–0.7042), positive εNd(t) (+4.6 to +5.1) and near-zero εHf(t) (0.0 to +0.3) values. Compared to the SW-Fuyun granite, the Halasu samples are featured by relatively higher $(^{87}Sr/^{86}Sr)_i$ (0.7035–0.7063), lower εNd(t) (+1.5 to +5.0) but similar εHf(t) (0.0 to +0.7) values. Different from the above two granites, the Kalasu granite has highly variable initial $^{87}Sr/^{86}Sr$ (0.7038–0.7244) and low εNd(t) (–3.7 to +1.4) but high εHf(t) (+3.6 to +8.7), similar to those of the middle Paleozoic granites in the Chinese Altai reported by Yu et al. (2017a) (Fig. 6a and b). Overall, the three Permian granites all show decoupling between Nd and Hf isotopic systems.

4.3.2. Triassic granitic intrusions

All the Triassic granites (Alaer, Xibuodu and Shangkelan) in this study possess variable initial $^{87}Sr/^{86}Sr$ ratios (0.6991–0.7381) (Fig. 6a). The Alaer granite shows variable εNd(t) (–3.9 to +4.7) as well as variable and positive εHf(t) (+1.7 to +12.0) values. In contrast, the Xibuodu and Shangkelan granites both have relatively uniform Nd–Hf isotopic compositions (Fig. 6b). In detail, the Xibuodu granite has εNd(t) and εHf(t) values being +1.9 to +2.4 and +6.5 to +7.3, respectively, and the Shangkelan granite has εNd(t) and εHf(t) values being –0.4 to +2.3 and +6.0 to +7.1, respectively. Moreover, the Triassic granites have Nd and Hf isotopic compositions within the range

of middle Paleozoic granites of the Chinese Altai as reported by Yu et al. (2017a). Similar to the case of the Permian granitic plutons, decoupling between Nd and Hf isotopic systems is also observed for the Triassic intrusions, but to a lesser degree (Fig. 6b).

5. Discussion

5.1. Effects of magmatic differentiation and alteration

During the evolution of felsic magmas, fractionation of various minerals such as amphibole, feldspar and biotite is common, which modifies the geochemical compositions of the remaining melts (Michael, 1983; Soesoo, 2000). Amphibole is enriched in middle REE (e.g., Dy) and its crystallization will introduce a decrease in Dy/Yb ratio (Castillo et al., 1999; Garrison and Davidson, 2003). Fractionation of feldspar will result in characteristic negative Eu anomalies, and crystallization of plagioclase and K-rich feldspar can be further differentiated by their tendency to deplete Sr and Sr–Ba, respectively (Defant and Drummond, 1993). Biotite is another possible crystallization phase, its fractionation will decrease Ba and Rb/Sr but slightly increase Sr in the residual magmas (Stepanov et al., 2014).

For the Permian granitic intrusions of this study, a positive correlation between $(Dy/Yb)_N$ and Mg# (Fig. 7a) is observed for samples from each individual intrusion and for all the intrusions, indicating extensive amphibole fractionation. They are also featured by significantly negative Eu anomalies (Fig. 5a), which can be ascribed to feldspar residue in the source or feldspar fractionation during the magma evolution.

Although the influence of feldspar residue in the source cannot be fully excluded, the negative correlations of Eu/Eu* with SiO_2 for the Permian granites (Fig. 7b) indicate that feldspar crystallization took place in the magmatic evolution. Furthermore, the positive correlation between Sr and Ba (Fig. 7c) suggests that K-rich feldspar is a major fractionation phase. As shown in Figure 7d, the strong increase in Rb/Sr ratios accompanied by slight decrease in Sr contents is consistent with removal of plagioclase.

For the Triassic granitic plutons, samples from individual pluton exhibit little variation in $(Dy/Yb)_N$ ratios but variable Mg# values (Fig. 7a), precluding significant crystallization of amphibole. Rocks from the Shangkelan and Xibuodo granites are characterized by markedly and slightly negative Eu anomalies, respectively (Fig. 5c), which, together with their constant Eu/Eu* ratios irrespective of SiO_2 contents (Fig. 7b), suggests that feldspar was a residual phase during their source melting. In the case of the Alaer granite, the rocks exhibit prominently negative Eu anomalies (Fig. 5c) as well as negative correlation of Eu/Eu* with SiO_2 and positive correlation of Sr with Ba (Fig. 7b and c), indicating extensive fractionation of K-rich feldspar. Plagioclase crystallization also occurred for the Triassic granites, as evidenced by the strongly negative correlation between Rb/Sr and Sr (Fig. 7d).

Some samples from the Permian and Triassic granites, especially those from the Shangkelan granite, have high ASI values (> 1.20), which can be caused by post-magmatic alteration. Therefore, it is necessary to evaluate the role of alteration on the high ASI values. The low LOI values (LOI < 1.7 wt%) as well as the lack of strong alteration minerals in thin sections do not support the alteration interpretation. In

addition, Ca- and Na-rich plagioclase is highly susceptive to alteration, while K-feldspar is less susceptive, leading to preferred loss of Ca and Na during moderate alteration and significant loss of K during strong alteration. In contrast, Al is highly resistant to alteration. Therefore, if alteration modified the chemical compositions of granitic rocks, the resulted rock series would form trends of Ca and Na removal on the Al–(Ca+Na)–K diagram (Nesbitt and Young, 1984). However, none of the Permian and Triassic granitic rocks form such a trend (Fig. 8). Instead, the samples show a narrow range of chemical alteration index, indicating that alteration did not play a major role on the high ASI values and other chemical compositions.

5.2. Petrogenesis

Granitic rocks can commonly be subdivided into A-, I- and S-type with distinct geochemical compositions and petrogenesis (Collins et al. 1982; Whalen et al., 1987; Chappell and White, 1992). A-type granites typically contain alkali mafic minerals such as Na-pyroxene (Wu et al., 2002). Geochemically, rocks of A-type granites are enriched in Zr, Nb, Ce and Y and have higher Fe/Mg or Ga/Al ratios, compared to I- and S-type granites (Whalen et al., 1987; Chappell and White, 1992; Bonin, 2007). In contrast, I-type granitoids often contain characteristic mineral of amphibole, and are featured by metaluminous to weakly peraluminous compostions with relatively low ASI values and negative correlation between P_2O_5 and SiO_2 contents (Chappell and White, 1992; Chappell, 1999). As for S-type graintes, they often contain characteristic minerals such as cordierite and muscovite, and are marked by strongly peraluminous compostions

with high ASI values (Chappell and White, 1992; Sylvester, 1998).

All the Permian and Triassic granitic intrusions in this study are characterized by low Ga/Al and FeO^T/MgO ratios as well as low contents of Zr + Nb + Ce + Y (Fig. 9a and b), clearly distinguishing them from A-type granitic rocks. Rocks from the Shangkelan granite are highly oversaturated in Al with ASI value up to 1.45 (Fig. 4d), indicating affinities to S-type granite. The remaining samples are featured by weakly to strongly peraluminous compositions with ASI values ranging from 1.02 to 1.19. On the other hand, the P_2O_5 contents of all the granitic samples decrease with increasing SiO_2 contents as illustrated in Figure 9c, indicating an affinity to I-type granite, which is consistent with the existence of amphibole fractionation for the Permian granitic samples. Overall, the above features reflect geochemical affinities of both S- and I-type granites, demonstrating that both meta-igneous and meta-sedimentary materials were involved in their sources.

In addition, all the granites of this study are geochemically similar to the HSGs described by Lee and Morton (2015) and Wu et al. (2017), including high SiO_2 (mostly higher than 70 wt.%) and high K_2O (mostly larger than 3.0 wt.%) contents. Previous petrological, geochemical and experimental studies indicated that such high-silica granitic magmas can be generated either by high degrees of magmatic differentiation (Michael, 1983; Glazner et al., 2008) or by partial melting within upper–lower crust depths (Gualda and Ghiorso, 2013; Lee and Morton, 2015).

5.2.1. Origin of Permian granitic intrusions

The Permian granitic rocks of this stuy are characterized by low Mg# (10.2–37.9) and low contents of Cr (<15 ppm) and Ni (<10 ppm), which are incompatible with a mantle contribution (Barbarin, 1996). Instead, low abundance of these elements reflect a crustal origin, which is supported by experimental results that melts of crustal materials generally have low Mg# (<40) (Patiño Douce and Johnston, 1991; Rapp and Watson, 1995). Melts of meta-igneous rocks are marked by high CaO and CaO/Na_2O but low Rb and Al_2O_3 as well as low Al_2O_3/TiO_2, Rb/Ba and Rb/Sr, while melts of sediment-rich sources display the opposite features (Sylvester, 1998; Jung and Pfänder, 2007). The three Permian granitic plutons of this study have variable Al_2O_3/TiO_2, Rb/Ba and Rb/Sr ratios (Fig. 10), indicating a mixed source involving meta-basaltic rocks and clay-poor sediments. In addition, some Permian granitic rocks have extremely high SiO_2 contents (up to 75.8 wt.%), higher than those (generally below 72 wt.%) of experimental melts of basaltic or sediment-rich sources (Patiño Douce and Johnston, 1991; Rapp and Watson, 1995), implying that fractionation of silica-poor minerals took place. This is in consistence with the differentiation of amphibole and feldspar as discussed in section 5.1.

The SW-Fuyun and Halasu granites have positive εNd(t) and εHf(t) values (Fig. 6), indicating that a juvenile crustal source played a crucial role in their petrogenesis (White and Hofmann, 1982; Bennett et al., 1993). However, samples from the Kalasu granite exhibit low εNd(t) (–3.6 to +1.4) but high εHf(t) (+3.8 to +8.8) values (Fig. 6), which may suggest some involvement of recycled sediment materials in the magma source. This inference is consistent with the fact that some samples from the Kalasu

granite show the highest Al_2O_3/TiO_2 and Rb/Sr ratios among the Permian granitic rocks (Fig. 10). In addition, the relatively lower εNd(t) but higher εHf(t) values compared to the terrestrial array (Fig. 6b) reflect the Nd–Hf isotopic decoupling, which can be explained by binary mixing between juvenile crust (represented by depleted mantle) and recycled sediments (represented by Habahe Group) (Fig. 10b). For the SW-Fuyun and Halasu granites, they show elevated εNd(t) relative to εHf(t) compared to the terrestrial array (Fig. 6b), probably suggesting that the involved juvenile crustal materials were derived from a source metasomatized by slab melts, because melts from subducted oceanic slabs introduce variable enrichment of incompatible elements in the overlying mantle wedge (e.g., Kempton et al., 1995; Rapp et al., 1999). During this process, Nd is preferentially transferred into slab-derived melts relative to Hf, which makes Nd isotopic systems more sensitive to metasomatism by slab melting (Hoffmann et al., 2011). Accordingly, melts from subducted slab will carry highly depleted Nd–Hf isotopic signatures with high concentrations of Nd but less concentrations of Hf, which will cause strong overprinting of depleted Nd isotopic signatures but weak overprinting of Hf isotopic signatures on the overlying lithosphere (Hoffmann et al., 2011). As a result, magmas originated from such a metasomatized source would have more depleted Nd but less influenced Hf isotopic compositions, leading to Nd–Hf isotopic decoupling.

In conclusion, the Permian granitic rocks of this study could be derived from a mixed source of juvenile mafic crust and recycled sediments, and underwent significant crystal fractionation. Source of the Kalasu granite involved relatively high proportions of sediments, while the SW-Fuyun and Halasu granites were mainly derived from meta-

igneous crust.

5.2.2. Origin of Triassic granitic intrusions

The Triassic granitic intrusions of this study possess high SiO_2 (71.0–77.2 wt.%) but low Mg# (<37.4), Cr (<47.0 ppm) and Ni (Ni< 6.9 ppm), suggesting a mainly crustal origin. Rocks from the Alaer and Xibuodu granites exhibit relatively low Al_2O_3/TiO_2, Rb/Ba and Rb/Sr ratios, indicating a mixed source of meta-basaltic crust and clay-poor sediments, while rocks from the Shangkelan granite display relatively high Al_2O_3/TiO_2, Rb/Ba and Rb/Sr ratios, implying a major origination from clay-rich sediments (Fig. 10), consistent with their high and variable ASI values (1.08–1.45). Similar to the Permian granitic samples, the Triassic granitic samples are featured by high-silica compositions (Fig. 4a). Nevertheless, relative to the Permian granites, the Triassic granites underwent less degrees of fractional crystallization, as discussed above, reflecting that their high-silica nature mainly resulted from relative shallow melting depths (Gualda and Ghiorso, 2013; Lee and Morton, 2015). Isotopically, the three Triassic granites have Nd and Hf isotopic compositions similar to those of the Permian Kalasu granite but with a less degree of decoupling (Fig. 6b). Such trend suggests that the Triassic granites were derived from a mixed source containing regional sediments (represented by the Habahe Group and Kangbutiebao Formation) and mafic crust.

5.3. Implications

By integrating published data for the Chinese Altai, two episodes of magmatism

after ca. 300 Ma have been recognized, one at 291–257 Ma and the other at 225–209 Ma (Fig. 11), as respectively represented by the Permian and Triassic granitoids in this study. Thereinto, the early Permian granites (291 Ma for the SW-Fuyun and 287 Ma for the Kalasu) investigated in this study exhibit characteristics of both volcanic arc granites and syn-collisional granites (Fig. 12a and b), indicating that the oceanic basin in the Chinese Altai was probably closed in the period of 298–292 Ma and thus provided the first constraint on the initial closure of the oceanic basin in the Chinese Altai. Subsequently, the Chinese Altai evolved into a post-collisional stage, which is supported by several other lines of evidence. For example, studies on Permian (287–260 Ma) A-type granitic and mafic rocks demonstrated that rocks emplaced in this period formed under a post-collisional extensional environment (Han et al., 2004; Chen and Han, 2006; Tong et al., 2006a, 2006b; Briggs et al., 2007; Zhang et al., 2012). Moreover, the ultra-high temperature metapelitic granulite (278 Ma) in the Chinese Altai has been ascribed to underplating and heating of mantle-derived mafic magmas in an anorogenic setting (Tong et al., 2014b). Therefore, magmatism posterior to 300 Ma was likely generated in a post-collisional or an anorogenic setting. Combing data of this study with those of previous studies, magmatic activities in the291–257 Ma and 225–209 Ma periods show contrasting rock assemblages and geochemical compositions, probably corresponding to the post-collision and intraplate stages, respectively, based on the following observations.

Firstly, Permian granitic rocks are distributed in the southern part of the Chinese Altai, especially along the Erqis fault, while Triassic granitic rocks occurred not only

in the southern but in the central and northern parts of the Chinese Altai (Fig. 1b). It is accepted that the Chinese Altai experienced southward accretion in the Paleozoic and the final suture is the Erqis fault in the south (Windley et al., 2007; Wang et al., 2009). Therefore, the generation of Permian granitic rocks along the Erqis fault is probably related to the post-collisional extension. On the other hand, the distribution of Triassic granitic rocks is likely controlled by an intra-plate tectonic regime.

Secondly, the Permian rocks are mostly I- and A-type granitoids with intensive mafic magmatism, while the Triassic rocks are mostly I- and S-type granites with little mafic volcanism (Wang et al., 2010; Yuan et al., 2011). The increasing S-type granites can be reflected by progressive increase in ASI values for granitic magmas (Fig. 11a). Relative to the Carboniferous to Permian felsic rocks, the Triassic felsic rocks show higher ASI values with most above 1.0, indicating a more peraluminous feature and a higher contribution of mature continental crust. Besides, reduced mafic magmatism reflects that the magmatic activities were shifted from mantle to continental crust.

Thirdly, the $K_2O + Na_2O$ and Th contents for the felsic rocks (Fig. 11b and c) are low in the late Carboniferous, but begin to increase in the early Permian and reach the peak in the Triassic. Such enrichment trends reflect progressively vanishing of juvenile materials but increasing of mature continental materials in the magma source, because K, Na and Th are incompatible and tend to enter into the mobile phases such as melts and thus accumulate within the continental crust, especially the upper crust (Hofmann, 1988; Rudnick and Gao, 2003). Thus, it can be concluded that melting of juvenile mafic crust was gradually replaced by reworking of evolved continental crust from early

Permian to Triassic in the Chinese Altai. This inference is further supported by the increasing $^{87}Sr/^{86}Sr$ ratios (Fig. 11d) for mafic and felsic rocks from late Carboniferous to Permian and Triassic, since evolved continental crust is featured by highly radiogenic Sr isotopes (Goldstein and Jacobsen, 1988; Jackson et al., 2007).

Fourthly, the V/Sc ratio of mafic magma is an effective proxy for redox-state in the mantle, and high V/Sc ratios reflect high fO_2 in the mantle source probably due to the intense metasomatism by subduction-originated fluids (Li et al., 2004; Lee et al., 2005). In the Chinese Altai, late Carboniferous and Permian mafic magmas exhibit a wide range of V/Sc ratios with some significantly higher than those of MORB, while the V/Sc ratios of Triassic mafic magmas are limited to MORB levels or lower (Fig. 11e). This shift indicates that little subduction-modified mantle was involved in the Triassic magmatic source compared to the late Carboniferous and Permian magmatic sources.

Fifthly, mature continental sediments develop through intense weathering and long-distance transportation and consist mainly of weathering-resistant minerals, which are poor in CaO and TiO_2 but rich in LILE such as Rb, and S-type granitoids with such sediments as the source will inherent similar attributions (Sylvester, 1998). For granitoids in the Chinese Altai, late Carboniferous granitoids are characterized by high CaO/Na_2O but low Al_2O_3/TiO_2, Rb/Ba and Rb/Sr ratios, and almost all plot into the range of basalt-derived granitic rocks (Fig. 12c and d). In contrast, the Permian granitoids fall into the ranges between basalt-derived and clay-poor sediment-derived granites, while the Triassic granitoids cover the widest range from basalt-derived to

clay-poor sediment-derived and clay-rich sediment-derived granites. Such trends reflect more and more strongly reworking of continental crustal materials, which led to the formation of voluminous Triassic granitoids.

Finally, high field strength elements and heavy REEs such as Nb, Ta, Y and Yb are enriched in intraplate felsic magmatism, while syn-collisional felsic magmatism is enriched in Rb. In contrast, volcanic arc-related felsic rocks are relatively depleted in both (Pearce et al., 1984). On the tectonic discrimination diagrams of Rb versus Y + Nb and Rb versus Yb + Ta (Fig. 12a and b), late Carboniferous felsic rocks fall in the field of volcanic arc granites, whereas the Permian and Triassic felsic rocks form an evolution curve which moves from volcanic arc towards syn-collisional and finally into the within-plate field.

Overall, the above geological facts imply that the oceanic basin in the Chinese Altai was probably closed in the latest Carboniferous, and subsequently this region experienced the tectonic transition from a post-collision to an intraplate setting from Permian to Triassic.

The HSGs with SiO_2 contents higher than 70 wt.% represent high levels of chemical differentiation of silicate earth. If the HSGs experience partial melting, the resulting melts are of similar compositions, especially silica contents, compared to their sources. Intensive re-melting of continental crust materials will create granitic rocks with high-silica nature, which are highly stable (Wu et al., 2017). Accordingly, the widespread high-silica magmas can be considered as a diagnostic characteristic of mature continental crust (Rudnick and Gao, 2003; Wu et al., 2017). In the Chinese Altai,

the HSGs widely occurred in the Permian and Triassic, and much more dominantly in the latter (Fig. 11f). As discussed in section 5.2, the Permian HSGs likely represent melting products of a mixed crustal source with significantly crystal fractionation, while the Triassic HSGs were most likely derived from high-silica crust sources such as silica-rich sediments with limited fractional crystallization.

In conclusion, the Permian and Triassic HSGs in the Chinese Altai may record the post-collision and intraplate settings, respectively. In addition to the HSGs, mafic magmatism was also widely developed in the Permian. However, little mafic magmatism occurred in the Triassic. The difference in mafic magmatic volume between Permian and Triassic can be ascribed to contrasting tectonic scales with the former extending across the lithosphere but the latter mostly limited to the continental crust. For the Permian HSGs, they were probably induced by underplating of mafic magmatism under a post-collisional extensional setting (Han et al., 2004; Chen and Han, 2006; Tong et al., 2006a, 2006b; Briggs et al., 2007; Zhang et al., 2012). On the other hand, the Triassic HSGs could be produced by frictional heating, since intense friction during the movement of fault surfaces could lead to heating (Obata and Karato, 1995; Andersen and Austrheim, 2006; Del Gaudio et al., 2009). This energy release may account for a significant proportion of total fault activity energy budget (Brown, 1998; Kanamori et al., 2001). In addition, the fault fractures also promote hydrous flow and lower the solidus of minerals, which can result in dehydration melting (Otsuki et al., 2003). Such an interpretation is supported by structural studies that the Erqis and Fuyun faults, as vitally structural elements the Chinese Altai, experienced intensive strike-slip

faulting in the Triassic (Briggs et al., 2007, 2009), which provided the possibility for heat accumulation by fault tectonism. Moreover, the small amount of Triassic mafic magmatism (exampled by the Ashele basalt, Yuan et al., 2011) may also indicate that underplating of mafic magmas played a certain role in the formation of the Triassic HSGs. As such, the post-collision and intraplate tectonic activities, especially the latter, could facilitate the generation of HSGs, which drove maturation of continental crust in accretionary orogenic belts.

6. Conclusions

Two periods (Permian and Triassic) of high-silica granites are recognized in the Chinese Altai. The former were generated by partial melting of a mixed crustal source, involving mainly juvenile crust and subordinate sediment, with significant crystal fractionation. In contrast, the latter were also formed by melting of a mixed crustal source, but containing mainly sediment and subordinate juvenile crust, without prominent crystal fractionation. Several lines of geological evidence imply that the granitoids of these two periods (Permian and Triassic) probably formed under post-collision and intraplate extensional settings, respectively. In addition, HSGs formed in these two stages, especially the latter stage, marked the maturation of continental crust in the Chinese Altai.

Acknowledgements

We thank Ms. Shengling Sun, and Mr. Xianglin Tu, Jinlong Ma and Le Zhang, for

their help with the geochemical analyses. We are grateful to Editor Meifu Zhou for his kind editorial help and constructive comments, and two anonymous reviewers, whose insightful and constructive reviews greatly improve this manuscript. This work was financially supported by the National Key R&D Program of China (2017YFC0601205), the National Science Foundation of China (41603030, 41573025), and the Hong Kong RGC research projects (17303415, 17302317). This is a contribution of the Chemical Geodynamic Joint Laboratory between HKU and GIG, CAS.

References

Andersen, T.B., 2002. Correction of common lead in U–Pb analyses that do not report ^{204}Pb. Chemical geology 192, 59–79.

Andersen, T.B., Austrheim, H., 2006. Fossil earthquakes recorded by pseudotachylytes in mantle peridotite from the Alpine subduction complex of Corsica. Earth and Planetary Science Letters 242, 58–72.

Bachmann, O., Bergantz, G.W., 2008. Rhyolites and their source mushes across tectonic settings. Journal of Petrology 49, 2277–2285.

Barbarin, B., 1996. Genesis of the two main types of peraluminous granitoids. Geology 24, 295–298.

Bennett, V.C., Nutman, A.P., McCulloch, M.T., 1993. Nd isotopic evidence for transient, highly depleted mantle reservoirs in the early history of the Earth. Earth and Planetary Science Letters 119, 299–317.

Black, R., Liegeois, J.P., 1993. Cratons, mobile belts, alkaline rocks and continental lithospheric mantle: the Pan-African testimony. Journal of the Geological Society 150, 89–98.

Bonin, B., 2004. Do coeval mafic and felsic magmas in post-collisional to within-plate regimes necessarily imply two contrasting, mantle and crustal, sources? A review. Lithos 78, 1–24.

Bonin, B., 2007. A-type granites and related rocks: evolution of a concept, problems and prospects. Lithos 97, 1–29.

Bonin, B., Azzouni-Sekkal, A., Bussy, F., Ferrag, S., 1998. Alkali-calcic and alkaline post-orogenic (PO) granite magmatism: petrologic constraints and geodynamic settings. Lithos 45, 45–70.

Briggs, S.M., Yin, A., Manning, C.E., Chen, Z.L., Wang, X.F., Grove, M., 2007. Late Paleozoic tectonic history of the Ertix Fault in the Chinese Altai and its implications for the development of the Central Asian Orogenic System. Geological Society of America Bulletin 119, 944–960.

Briggs, S.M., Yin, A., Manning, C.E., Chen, Z.L., Wang, X.F., 2009. Tectonic development of the southern Chinese Altai Range as determined by structural geology, thermobarometry, $^{40}Ar/^{39}Ar$ thermochronology, Th/Pb ion-microprobe monazite geochronology. Geological Society of America Bulletin 121, 1381–1393.

Brown, S.R., 1998. Frictional heating on faults: Stable sliding versus stick slip. Journal of Geophysical Research: Solid Earth 103, 7413–7420.

Buslov, M.M., Watanabe, T., Fujiwara, Y., Iwata, K., Smirnova, L.V., Safonova, I.Y., Semakov, N.N., Kiryanova, A.P., 2004. Late Paleozoic faults of the Altai region, Central Asia: tectonic pattern and model of formation. Journal of Asian Earth Sciences 23, 655–671.

Cai, K.D., Yuan, C., Sun, M., Xiao, W.J., Chen, H.L., Long, X.P., Zhao, Y.J., Li, J.L., 2007. Geochemical characteristics and ^{40}Ar–^{39}Ar ages of the amphibolites and gabbros in Tarlang area: implications for tectonic evolution of the Chinese Altai. Acta Petrologica Sinica 23, 877–888.

Cai, K., Sun, M., Yuan, C., Long, X., Xiao, W., 2011. Geological framework and Paleozoic tectonic history of the Chinese Altai, NW China: a review. Russian Geology and Geophysics 52, 1619–1633.

Castillo, P.R., Janney, P.E., Solidum, R.U., 1999. Petrology and geochemistry of Camiguin Island, southern Philippines: insights to the source of adakites and other lavas in a complex arc setting. Contributions to Mineralogy and Petrology 134, 33–51.

Chai, F., Mao, J., Dong, L., Yang, F., Liu, F., Geng, X., Zhang, Z. 2009. Geochronology of metarhyolites from the Kangbutiebao Formation in the Kelang basin, Altay Mountains, Xinjiang: implications for the tectonic evolution and metallogeny. Gondwana Research 16, 189–200.

Chappell, B.W., 1999. Aluminium saturation in I- and S-type granites and the characterization of fractionated haplogranites. Lithos 46, 535–551.

Chappell, B.W., White, A.J.R., 1992. I- and S-type granites in the Lachlan Fold Belt. Earth and Environmental Science Transactions of the Royal Society of Edinburgh 83, 1–26.

Chen, B., Jahn, B.M., 2002. Geochemical and isotopic studies of the sedimentary and granitic rocks of the Altai orogen of northwest China and their tectonic implications. Geological Magazine 39, 1–13.

Chen, F.W., Li, H.Q., Lu, Y.F., 2002. Temporo–spatial distribution of rare metal and REE deposits in Xinjiang, Northwest China. Acta Geologica Sinica 76, 478–487.

Chen, L., Han, B., 2006. Geochronology, geochemistry and Sr–Nd–Pb isotopic composition of mafic intrusive rocks in Wuqiagou area, north Xinjiang: constraints for mantle sources and deep processes. Acta Petrologica et Mineralogica 22, 1201–1214.

Collins, W.J., Beams, S.D., White, A.J.R., Chappell, B.W., 1982. Nature and origin of A-type granites with particular reference to southeastern Australia. Contributions to mineralogy and petrology 80, 189–200.

Cox, K.G., Bell, J.D., Goscombe, B., 1979, The interpretation of igneous rocks. London: G. Allen and Unwin.

Defant, M.J., Drummond, M.S., 1993. Mount St. Helens: potential example of the partial melting of the subducted lithosphere in a volcanic arc. Geology 21, 547–550.

Del Gaudio, P., Di Toro, G., Han, R., Hirose, T., Nielsen, S., Shimamoto, T., Cavallo, A., 2009. Frictional melting of peridotite and seismic slip. Journal of Geophysical Research: Solid Earth 114, 1–19.

Duggen, S., Hoernle, K., van den Bogaard, P., Garbe-Schönberg, D., 2005. Post-collisional transition from subduction-to intraplate-type magmatism in the westernmost Mediterranean: evidence for continental-edge delamination of subcontinental lithosphere. Journal of Petrology 46, 1155–1201.

Eby, G.N., 1992. Chemical subdivision of the A-type granitoids: petrogenetic and tectonic implications. Geology 20, 641–644.

Ewing, R.C., Meldrum, A., Wang, L., Weber, W.J., Corrales, L.R., 2003. Radiation effects in zircon. Reviews in Mineralogy and geochemistry 53, 387–425.

Garrison, J.M., Davidson, J.P., 2003. Dubious case for slab melting in the Northern volcanic zone of the Andes. Geology 31, 565–568.

Gerdes, A., Wörner, G., Henk, A., 2000. Post-collisional granite generation and HT–LP metamorphism by radiogenic heating: the Variscan South Bohemian Batholith. Journal of the Geological Society 157, 577–587.

Glazner, A.F., Coleman, D.S., Bartley, J.M., 2008. The tenuous connection between high-silica rhyolites and granodiorite plutons. Geology 36, 183–186.

Goldstein, S.J., Jacobsen, S.B., 1988. Nd and Sr isotopic systematics of river water suspended material: implications for crustal evolution. Earth and Planetary Science Letters 87, 249–265.

Gualda, G.A., Ghiorso, M.S., 2013. Low-pressure origin of high-silica rhyolites and granites. The Journal of Geology 121, 537–545.

Han, B., Ji, J., Song, B., Chen, L., Li, Z., 2004. SHIMP zircon U–Pb age of Kalatongke No.1 and Huangshandong Cu–Ni-bearing mafic-ultramafic complexes, North Xinjiang, and geological implications. Chinese Science Bulletin 49, 2424–2429.

Han, C., Xiao, W., Zhao, G., Qu, W., Du, A., 2007. Re–Os dating of the Kalatongke Cu–Ni deposit, Altay Shan, NW China, and resulting geodynamic implications. Ore Geology Reviews 32, 452–468.

Hofmann, A.W., 1988. Chemical differentiation of the Earth: the relationship between mantle, continental crust, and oceanic crust. Earth and Planetary Science Letters 90, 297–314.

Hoffmann, J.E., Münker, C., Polat, A., Rosing, M.T., Schulz, T., 2011. The origin of decoupled Hf–Nd isotope compositions in Eoarchean rocks from southern West Greenland. Geochimica et Cosmochimica Acta 75, 6610–6628.

Jackson, M.G., Hart, S.R., Koppers, A.A., Staudigel, H., Konter, J., Blusztajn, J., Kurz, M., Russell, J.A., 2007. The return of subducted continental crust in Samoan lavas. Nature 448, 684–687.

Jahn, B.M., Wu, F., Chen, B., 2000. Granitoids of the Central Asian Orogenic Belt and continental growth in the Phanerozoic. Earth and Environmental Science Transactions of the Royal Society of Edinburgh 91, 181–193.

Janoušek, V., Holub, F.V., 2007. The causal link between HP-HT metamorphism and ultrapotassic magmatism in collisional orogens: case study from the Moldanubian Zone of the Bohemian Massif. Proceedings of the Geologists' Association 118, 75–86.

Jung, S., Pfänder, J.A., 2007. Source composition and melting temperatures of orogenic granitoids: constraints from CaO/Na_2O, Al_2O_3/TiO_2 and accessory mineral saturation thermometry.

European Journal of Mineralogy 19, 859–870.

Kanamori, H., Teisseyre, R., Majewski, E., 2001. Energy budget of earthquakes and seismic efficiency. Earthquake Thermodynamics and Phase Transformations in the Earth's Interior 76, 293–305.

Kempton, P.D., Downes, H., Sharkov, E.V., Vetrin, V.R., Ionov, D.A., Carswell, D.A., Beard, A., 1995. Petrology and geochemistry of xenoliths from the Northern Baltic shield: evidence for partial melting and metasomatism in the lower crust beneath an Archaean terrane. Lithos 36, 157–184.

Lee, C.T.A., Leeman, W.P., Canil, D., Li, Z.X.A., 2005. Similar V/Sc systematics in MORB and arc basalts: implications for the oxygen fugacities of their mantle source regions. Journal of Petrology 46, 2313–2336.

Lee, C.T.A., Morton, D.M., 2015. High silica granites: Terminal porosity and crystal settling in shallow magma chambers. Earth and Planetary Science Letters 409, 23–31.

Liegeois, J.P., Navez, J., Hertogen, J., Black, R., 1998. Contrasting origin of post-collisional high-K calc-alkaline and shoshonitic versus alkaline and peralkaline granitoids. The use of sliding normalization. Lithos 45, 1–28.

Li, X.H., Li, Z.X., Wingate, M.T., Chung, S.L., Liu, Y., Lin, G.C., Li, W.X., 2006. Geochemistry of the 755 Ma Mundine Well dyke swarm, northwestern Australia: Part of a Neoproterozoic mantle superplume beneath Rodinia?. Precambrian Research 146, 1–15.

Li, Z.X.A., Lee, C.T.A., 2004. The constancy of upper mantle fO_2 through time inferred from V/Sc ratios in basalts. Earth and Planetary Science Letters 228, 483–493.

Liu, F., Li, Y.H., Mao, J.W., Yang, F.Q., Chai, F.M., Geng, X.X., Yang, Z.X., 2008. SHRIMP U–Pb Ages of the Abagong granites in the Altay orogen and their geological implications. Acta Geoscientica Sinica 29, 795–804.

Liu, F., Zhang, Z.X., Li, Q., Zhang, C., Li, C., 2014. New precise timing constraint for the Keketuohai No. 3 pegmatite in Xinjiang, China, and identification of its parental pluton. Ore Geology Reviews 56, 209–219.

Lin, J., Liu, Y., Yang, Y, Hu, Z., 2016. Calibration and correction of LA-ICP-MS and LA-MC-ICP-MS analyses for element contents and isotopic ratios. Solid Earth Sciences 1, 5–27.

Liu, W., Liu, X.J., Xiao, W.J., 2012. Massive granitoid production without massive continental-

crust growth in the Chinese Altay: Insight into the source rock of granitoids using integrated zircon U-Pb age, Hf-Nd-Sr isotopes and geochemistry. American Journal of Science 312, 629–684.

Long, X., Sun, M., Yuan, C., Xiao, W., Lin, S., Wu, F., Xia, X.P., Cai, K., 2007. Detrital zircon age and Hf isotopic studies for metasedimentary rocks from the Chinese Altai: Implications for the Early Paleozoic tectonic evolution of the Central Asian Orogenic Belt. Tectonics 26, 1–20.

Ludwig, K.R., 2003. Isoplot 3.00: A geochronological toolkit for Microsoft Excel. Berkeley Geochronology Center Special Publication 4, 1–70.

Michael, P.J., 1983. Chemical differentiation of the Bishop Tuff and other high-silica magmas through crystallization processes. Geology 11, 31–34.

Nesbitt, H.W., Young, G.M., 1984. Prediction of some weathering trends of plutonic and volcanic rocks based on thermodynamic and kinetic considerations. Geochimica et Cosmochimica Acta 48, 1523–1534.

Nikishin, A.M., Ziegler, P.A., Abbott, D., Brunet, M.F., Cloetingh, S., 2002. Permo–Triassic intraplate magmatism and rifting in Eurasia: implications for mantle plumes and mantle dynamics. Tectonophysics 351, 3–39.

Obata, M., Karato, S.I., 1995. Ultramafic pseudotachylite from the Balmuccia peridotite, Ivrea–Verbano zone, northern Italy. Tectonophysics 242, 313–328.

Otsuki, K., Monzawa, N., Nagase, T., 2003. Fluidization and melting of fault gouge during seismic slip: Identification in the Nojima fault zone and implications for focal earthquake mechanisms. Journal of Geophysical Research: Solid Earth 108, 1–18.

Patiño Douce, A.E., Johnston, A.D., 1991. Phase equilibria and melt productivity in the pelitic system: implications for the origin of peraluminous granitoids and aluminous granulites. Contributions to Mineralogy and Petrology 107, 202–218.

Pearce, J.A., Harris, N.B., Tindle, A.G., 1984. Trace element discrimination diagrams for the tectonic interpretation of granitic rocks. Journal of petrology 25, 956–983.

Peccerillo, A., Taylor, S.R., 1976. Geochemistry of Eocene calc-alkaline volcanic rocks from the Kastamonu area, northern Turkey. Contributions to mineralogy and petrology 58, 63–81.

Rapp, R.P., Watson, E.B., 1995. Dehydration melting of metabasalt at 8–32 kbar: implications for continental growth and crust-mantle recycling. Journal of Petrology 36, 891–931.

Rapp, R.P., Shimizu, N., Norman, M.D., Applegate, G.S., 1999. Reaction between slab-derived melts and peridotite in the mantle wedge: experimental constraints at 3.8 GPa. Chemical Geology 160, 335–356.

Rudnick, R.L., Gao, S., 2003. Composition of the continental crust. Treatise on geochemistry 3, 1–64.

Salters, V.J., Stracke, A., 2004. Composition of the depleted mantle. Geochemistry, Geophysics, Geosystems 5, 1–27.

Sengör, A.M.C., Natal'In, B.A., Burtman, V.S., 1993. Evolution of the Altaid tectonic collage and Palaeozoic crustal growth in Eurasia. Nature 364, 299–307.

Sengör, A.M.C., Natal'In, B.A., 1996. Turkic-type orogeny and its role in the making of the continental crust. Annual Review of Earth and Planetary Sciences 24, 263–337.

Sheldrick, T.C., Barry, T.L., Van Hinsbergen, D.J., Kempton, P.D., 2018. Constraining lithospheric removal and asthenospheric input to melts in Central Asia: A geochemical study of Triassic to Cretaceous magmatic rocks in the Gobi Altai (Mongolia). Lithos 296, 297–315.

Soesoo, A., 2000. Fractional crystallization of mantle-derived melts as a mechanism for some I-type granite petrogenesis: an example from Lachlan Fold Belt, Australia. Journal of the Geological Society 157, 135–149.

Stepanov, A., Mavrogenes, J.A., Meffre, S., Davidson, P., 2014. The key role of mica during igneous concentration of tantalum. Contributions to Mineralogy and Petrology 167, 1–8.

Sun, M., Yuan, C., Xiao, W., Long, X., Xia, X., Zhao, G., Lin, S.F., Wu, F.Y., Kröner, A., 2008. Zircon U–Pb and Hf isotopic study of gneissic rocks from the Chinese Altai: progressive accretionary history in the early to middle Palaeozoic. Chemical Geology 247, 352–383.

Sylvester, P.J., 1998. Post-collisional strongly peraluminous granites. Lithos 45, 29–44.

Sun, S.S., McDonough, W.F., 1989. Chemical and isotopic systematics of oceanic basalts: implications for mantle composition and processes. Geological Society, London, Special Publications 42, 313–345.

Tadayon, M., Rossetti, F., Zattin, M., Nozaem, R., Calzolari, G., Madanipour, S., Salvini, F., 2017. The post-Eocene evolution of the Doruneh Fault region (central Iran): The intraplate response to the Reorganization of the Arabia-Eurasia collision zone. Tectonics 36, 3038–3064.

Tong Y., 2006. Geochronology, Origin of the Late Paleozoic Granitoids from the Altai Orogen in

China and Their Geological Significance: Beijing, China, Chinese Academy of Geological Sciences. Unpublished Ph. D. Thesis.

Tong, Y., Hong, D., Wang, T., Wang, S., Han, B., 2006a. TIMS U–Pb zircon ages of Fuyun post-orogenic linear granite plutons on the southern margin of Altay orogenic belt and their implications. Acta Petrologica et Mineralogica 25, 85–89.

Tong, Y., Wang, T., Hong, D., Han, B., 2006b. Pb isotopic compositions of granitoids from the Altay Orogen (China): evidence for mantle-derived origin and continental growth. Acta Geologica Sinica 40, 517–528.

Tong, Y., Wang, T., Jahn, B.M., Sun, M., Hong, D.W., Gao, J.F., 2014a. Post-accretionary Permian granitoids in the Chinese Altai orogen: geochronology, petrogenesis and tectonic implications. American Journal of Science 314, 80–109.

Tong, L., Xu, Y.G., Cawood, P.A., Zhou, X., Chen, Y., Liu, Z., 2014b. Anticlockwise PT evolution at ~280 Ma recorded from ultrahigh-temperature metapelitic granulite in the Chinese Altai orogenic belt, a possible link with the Tarim mantle plume?. Journal of Asian Earth Sciences 94, 1–11.

Vervoort, J.D., Patchett, P.J., Blichert-Toft, J., Albarede, F., 1999. Relationships between Lu–Hf and Sm–Nd isotopic systems in the global sedimentary system. Earth and Planetary Science Letters 168, 79–99.

Wan, B., Xiao, W., Windley, B.F., Yuan, C., 2013. Permian hornblende gabbros in the Chinese Altai from a subduction-related hydrous parent magma, not from the Tarim mantle plume. Lithosphere 5, 290–299.

Wang, T., Hong, D.W., Tong, Y., Han, B.F., Shi, Y.R., 2005. Zircon U–Pb SHRIMP age and origin of post-orogenic Lamazhou granitic pluton from Chinese Altai Orogen: its implications for vertical continental growth. Acta Petrologica Sinica 21, 640–650.

Wang, T., Tong, Y., Jahn, B.M., Zou, T.R., Wang, Y.B., Hong, D.W., Han, B.F., 2007. SHRIMP U–Pb Zircon geochronology of the Altai No. 3 Pegmatite, NW China, its implications for the origin and tectonic setting of the pegmatite. Ore geology reviews 32, 325–336.

Wang, T., Li, W.P., Li, J.B., Hong, D.W., Tong, Y., 2008. Increase of juvenal mantle-derived composition from syn-orogenic to post-orogenic granites of the east part of the east Tian Shan (China) and implications for continental vertical growth: Sr and Nd isotopic evidence. Acta

Petrologica Sinica 24, 763–772.

Wang, T., Jahn, B.M., Kovach, V.P., Tong, Y., Hong, D.W., Han, B.F., 2009. Nd–Sr isotopic mapping of the Chinese Altai and implications for continental growth in the Central Asian Orogenic Belt. Lithos 110, 359–372.

Wang, T., Tong, Y., Li, S., Zhang, J.J., Shi, X.J., Li, J.Y., Han, B.F., Hong, D.W., 2010. Spatial and temporal variations of granitoids in the Altay orogen and their implications for tectonic setting and crustal growth: perspectives from Chinese Altay. Acta Petrologica et Mineralogica 29, 595–618.

Wang, Y., Yuan, C., Long, X., Sun, M., Xiao, W., Zhao, G., Cai, K., Jiang, Y., 2011. Geochemistry, zircon U–Pb ages and Hf isotopes of the Paleozoic volcanic rocks in the northwestern Chinese Altai: petrogenesis and tectonic implications. Journal of Asian Earth Sciences 42, 969–985.

Wei, G., 2002. Precise measurement of Sr isotopic composition of liquid and solid base using (LP) MC-ICPMS. Geochimica 31, 295–299.

Whalen, J.B., Currie, K.L., Chappell, B.W., 1987. A-type granites: geochemical characteristics, discrimination and petrogenesis. Contributions to mineralogy and petrology 95, 407–419.

White, W.M., Hofmann, A.W., 1982. Sr and Nd isotope geochemistry of oceanic basalts and mantle evolution. Nature 296, 821–825.

Willner, A.P., Richter, P.P., Ring, U., 2009. Structural overprint of a late Paleozoic accretionary system in north-central Chile (34°–35°S) during post-accretional deformation. Andean Geology 36, 17–36.

Windley, B.F., Kröner, A., Guo, J., Qu, G., Li, Y., Zhang, C., 2002. Neoproterozoic to Paleozoic geology of the Altai orogen, NW China: new zircon age data and tectonic evolution. The Journal of Geology 110, 719–737.

Wu, F.Y., Sun, D.Y., Li, H., Jahn, B.M., Wilde, S., 2002. A-type granites in northeastern China: age and geochemical constraints on their petrogenesis. Chemical Geology 187, 143–173.

Wu, F., Liu, X., Ji, W., Wang, J., Yang, L., 2017. Highly fractionated granites: Recognition and research. Science China Earth Sciences 60, 1201–1219.

Xiao, W., Windley, B.F., Badarch, G., Sun, S., Li, J., Qin, K., Wang, Z., 2004. Palaeozoic accretionary and convergent tectonics of the southern Altaids: implications for the growth of Central Asia. Journal of the Geological Society 161, 339–342.

Xue, C.J., Zhao, Z.F., Wu, G.G., 2010. The multi-periodic superimposed porphyry copper mineralization in Central Asian Tectonic Region: A case study of geology, geochemistry and chronology of Halasu copper deposit, Southeastern Altai, China. Earth Science Frontiers 17, 53–82.

Yuan, C., Sun, M., Long, X.P., Xia, X.P., Xiao, W.J., Li, X.H., Lin, S.F., Cai, K.D., 2007a. Constraining the deposition time and tectonic background of the Habahe Group of the Altai. Acta Petrologica et Mineralogica 237, 1635–1644.

Yuan, C., Sun, M., Xiao, W., Li, X., Chen, H., Lin, S., Xia, X., Long, X., 2007b. Accretionary orogenesis of the Chinese Altai: insights from Paleozoic granitoids. Chemical Geology 242, 22–39.

Yuan, C., Sun, M., Xu, Y., Zhao, G., Xiao, W., Long, X., Yin, J. 2011. Oceanic lithospheric mantle beneath the continental crust of the Chinese Altai. Journal of the geological society 168, 995–1000.

Yu, Y., Sun, M., Huang, X.L., Zhao, G., Li, P., Long, X., Cai, K., Xia, X., 2017a. Sr-Nd-Hf-Pb isotopic evidence for modification of the Devonian lithospheric mantle beneath the Chinese Altai. Lithos 284, 207–221.

Yu, Y., Sun, M., Long, X., Li, P., Zhao, G., Kröner, A., Broussolle, A., Yang, J., 2017b. Whole-rock Nd–Hf isotopic study of I-type and peraluminous granitic rocks from the Chinese Altai: constraints on the nature of the lower crust and tectonic setting. Gondwana Research 47, 131–141.

Zhang, C.L., Li, Z.X., Li, X.H., Xu, Y.G., Zhou, G., Ye, H.M., 2010. A Permian large igneous province in Tarim and Central Asian orogenic belt, NW China: Results of a ca. 275 Ma mantle plume?. GSA Bulletin 122, 2020–2040.

Zhang, C.L., Santosh, M., Zou, H.B., Xu, Y.G., Zhou, G., Dong, Y.G., Ding, R.F., Wang, H.Y., 2012. Revisiting the ‘‘Irtish tectonic belt’’: implications for the Palaeozoic tectonic evolution of the Altai orogen. Journal of Asian Earth Sciences 52, 117–133.

Zhang, C.L., Zou, H.B., Yao, C.Y., Dong, Y.G., 2014. Origin of Permian gabbroic intrusions in the southern margin of the Altai Orogenic belt: a possible link to the Permian Tarim mantle plume?. Lithos 204, 112–124.

Zhang, Y.Y., Sun, M., Yuan, C., Long, X.P., Jiang, Y.D., Li, P.F., Huang, Z.Y., Du, L., 2018.

Alternating trench advance and retreat: Insights from Paleozoic magmatism in the eastern Tianshan, Central Asian Orogenic Belt. Tectonics 37, 2142–2164.

Zhou, G., Zhang, Z.C., Zhang, X.L., Luo, S.B, Yang, W.P., Gu, G.Z., Wang, X., 2005. Discovery of Metabasic Rocks at the South Side of Mayinebo Fault in the South Margin of Altay Mountains, Xinjiang, and Its Geological Implications. Earth Science-Journal of China University of Geosciences 30, 738–746.

Zindler, A., Hart, S., 1986. Chemical geodynamics. Annual review of earth and planetary sciences 1, 493–571.

Figure captions:

Fig. 1. Tectonic sketch of the Central Asian Orogenic Belt (a) and Chinese Altai (b), modified after Jahn et al. (2000) and Windley et al. (2002), respectively. Bold numbers are indexes of units following the tectonic segmentation scheme of Windley et al. (2002): (1) Altaishan; (2) NW-Altaishan; (3) Central Altaishan; (4) Qingkuer–Abagong; (5) Erqis; (6) Perkin–Ertai. Colour arrows point to locations of early Carboniferous to Permian and Triassic granitic intrusions, with their ages (Ma) given at the end of arrows: (a) Jangjunshan; (b, e, g, i) Keketuohai pegmatite; (c) Shangkelan; (d, f) Alaer; (h) Halasu porphyry; (j) Kalasu; (k) Fuyun; (l) Shaerbulake; (m) Buerjin; (n) Lamazhao; (o) Erqis; (p) Xibuodu; (q) Fuyun gabbro; (r) Fuyun biotite granite; (s, t) Mayinerbo; (u) Takeshi; (v) Ashele granodiorite; (w) S. Altai diorite; (x) Buergen. (Chen and Jahn, 2002; Wang et al., 2005, 2007, 2008, 2009; Tong, 2006; Tong et al., 2006a, 2006b; Briggs et al., 2007; Yuan et al., 2007a, 2007b; Zhou et al., 2005; Liu et al., 2008; Sun et al., 2008; Xue et al., 2010)

Fig. 2. Field photos and cross-polarized microscopic views of Permian and Triassic granites the Chinese Altai.

Fig. 3. Zircon U–Pb concordia diagrams of the granitic intrusions in the Chinese Altai. Red ellipses represent valid zircon grains used for calculation of rock formation ages.

Fig. 4. Major element diagrams for the Chinese Altai granitic intrusions: (a) Total alkali–Silica (after Cox et al., 1979); (b) K_2O–SiO_2 (after Peccerillo and Taylor, 1976); (c) Mg#–SiO_2; (d) A/NK–ASI. Data for the Halasu granite are from Tong (2006) and data for the Shangkelan granite are from Tong et al. (2014a).

Fig. 5. (a) and (c) Chondrite normalized REE patterns. (b) and (d) primitive-mantle normalized trace element spider diagrams. Normalization data from Sun and McDonough (1989). Some data for the Halasu granite are from Tong (2006).

Fig. 6. Isotopic diagrams of the Chinese Altai granitic intrusions. (a) $\varepsilon Nd(t)$–$(^{87}Sr/^{86}Sr)_i$ (after Zindler and Hart, 1986) and (b) $\varepsilon Hf(t)$–$\varepsilon Nd(t)$ (after Vervoort et al., 1999; Salters and Stracke, 2004). Whole-rock $\varepsilon Nd(t)$ values for regional sediments represented as vertical bars in (b) are from Liu et al. (2012).

Fig. 7. (a) $(Dy/Yb)_N$–Mg#, (b) Eu/Eu*–SiO_2, (c) Sr–Ba and (d) Rb/Sr–Sr diagrams for the Chinese Altai granitic intrusions.

Fig. 8. Al–(Ca+Na)–K tertiary diagram for the granitic intrusions in the Chinese Altai (after Nesbitt and Young, 1984)

Fig. 9. (a) Y–Ga/Al (after Whalen et al., 1987), (b) FeO^T/MgO–(Zr + Nb + Ce + Y) (after Whalen et al., 1987) and (c) P_2O_5–SiO_2 diagrams for the Chinese Altai granitic intrusions.

Fig. 10. (a) CaO/Na_2O–Al_2O_3/TiO_2 (after Jung and Pfänder, 2007) and (b) Rb/Ba–Rb/Sr (after Sylvester, 1998) source discrimination diagrams for the Permian and Triassic granitic rocks in the Chinese Altai.

Fig. 11. Varied geochemical indicators through time from Carboniferous to Triassic in the Chinese Altai. (a) ASI; (b) Na_2O+K_2O; (c) Th; (d) $(^{87}Sr/^{86}Sr)_i$; (e) V/Sc and (f) SiO_2. The V/Sc field for MORB is from Lee et al. (2005). In addition to data in this study, data for felsic rocks in the Chinese Altai from those references listed in Fig. 1, and data for mafic rocks from Cai et al. (2007), Han et al. (2007), Zhang et al. (2010, 2014), Yuan et al. (2011), Wan et al. (2013) and Sheldrick et al. (2018) are also used for comparison.

Fig. 12. (a) Rb–(Y + Nb) and (b) Rb–(Yb + Ta) tectonic discrimination diagrams (after Pearce et al., 1984) and (c) CaO/Na_2O–Al_2O_3/TiO_2 (after Jung and Pfänder, 2007), (d) Rb/Ba–Rb/Sr (after Sylvester, 1998) source discrimination diagrams for the Chinese

Altai felsic rocks. Dataset used is the same as in Fig. 10.

Table 1 Bulk-rock major oxide (wt.%) compositions of the Chinese Altai granites

Sample	SW-Fuyun			Kalasu					Halasu	
	FY-2	FY-4	FY-7	KLS-1	KLS-2	KLS-3	KLS-4	KLS-5	HLS-5	3081*
SiO_2	73.8	73.9	73.9	72.2	72.8	75.8	72.2	72.0	71.9	70.3
TiO_2	0.17	0.16	0.17	0.12	0.12	0.07	0.25	0.24	0.32	0.41
Al_2O_3	13.6	13.4	13.5	14.7	14.5	12.8	14.1	14.5	13.9	14.6
$Fe_2O_3^T$	1.83	1.72	1.77	1.85	1.91	1.57	2.42	2.35	2.60	2.93
MnO	0.04	0.04	0.04	0.07	0.07	0.05	0.10	0.10	0.05	0.04
MgO	0.52	0.47	0.49	0.41	0.41	0.09	0.41	0.42	0.66	0.87
CaO	1.00	1.07	1.04	0.78	0.77	0.20	1.42	1.39	1.71	1.95
Na_2O	3.52	3.40	3.46	3.46	3.41	3.78	3.72	3.78	3.64	3.35
K_2O	4.55	4.51	4.53	4.55	4.65	4.88	4.24	4.50	3.90	4.03
P_2O_5	0.07	0.06	0.07	0.34	0.33	0.01	0.11	0.11	0.21	0.31
L.O.I	0.82	0.80	0.81	0.98	0.95	0.49	0.34	0.44	0.58	0.60
Total	99.9	99.6	99.8	99.4	99.9	99.7	99.3	99.8	99.4	99.4
Mg#	36	35	35	31	30	10	25	26	34	37

Sample	Halasu			Shangkelan					Alaer
	3082*	3083*	3084*	SKL-3	3212^	3214^	3211^	32112^	XSK-2^	ALR-1
SiO_2	70.9	71.7	67.6	77.2	73.8	75.7	74.6	76.1	73.9	72.4
TiO_2	0.34	0.36	0.69	0.08	0.22	0.11	0.22	0.10	0.08	0.16
Al_2O_3	14.5	14.5	15.0	12.6	13.9	13.4	13.3	13.0	14.3	13.8
$Fe_2O_3^T$	2.57	2.67	4.33	0.72	1.55	0.79	1.86	1.86	0.85	2.46
MnO	0.04	0.05	0.11	0.03	0.04	0.04	0.24	0.10	0.05	0.10
MgO	0.79	0.68	0.91	0.06	0.26	0.22	0.29	0.56	0.12	0.46
CaO	1.51	1.44	1.71	0.35	0.44	0.08	0.06	0.03	0.05	1.64
Na_2O	3.22	3.26	4.53	4.29	4.50	3.76	2.80	3.41	5.45	3.48
K_2O	4.37	4.13	3.48	3.67	4.22	4.74	5.16	3.02	1.17	4.08
P_2O_5	0.27	0.22	0.32	0.01	0.07	0.03	0.04	0.03	0.19	0.07
L.O.I	0.73	0.60	0.72	0.63	0.68	0.65	1.40	1.70	0.65	0.45
Total	99.3	99.4	99.4	99.7	99.7	99.5	99.9	99.8	96.8	99.1
Mg#	38	30	29	14	25	35	24	37	22	27

Sample	Alaer					Xibuodu		
	ALR-2	ALR-3	ALR-4	ALR-5	ALR-6	XBD-1	XBD-2	XBD-3
SiO_2	73.2	71.4	72.5	74.0	71.0	71.1	72.2	72.2
TiO_2	0.17	0.26	0.25	0.10	0.25	0.31	0.21	0.20
Al_2O_3	13.9	14.4	14.2	14.0	14.1	14.3	14.3	14.3
$Fe_2O_3^T$	2.23	3.29	3.07	1.72	2.31	2.51	2.45	2.45
MnO	0.08	0.10	0.10	0.07	0.08	0.07	0.09	0.09
MgO	0.48	0.67	0.64	0.19	0.52	0.55	0.49	0.43

CaO	1.58	2.23	2.21	1.04	1.17	1.51	1.47	1.55
Na_2O	3.51	3.42	3.47	3.06	2.68	3.56	3.55	3.42
K_2O	4.21	3.49	2.85	4.40	6.78	4.18	3.88	4.13
P_2O_5	0.06	0.11	0.08	0.19	0.22	0.18	0.18	0.14
L.O.I	0.58	0.25	0.45	0.72	0.45	0.40	0.62	0.78
Total	100.0	99.6	99.8	99.4	99.6	98.7	99.5	99.7
Mg#	30	29	29	18	31	30	28	26

Notes: Mg# = 100*Mg/(Mg+Fe^{2+}), assuming Fe^{2+}/Fe^{total} = 0.90; L.O.I = loss of ignition; $Fe_2O_3^T$ represents total Fe oxides as Fe_2O_3. Samples marked with * are from Tong (2006). Samples marked with **^** are from Tong et al. (2014a).

Table 2 Bulk-rock trace element (ppm) abundances for the Chinese Altai granites

Sample	SW-Fuyun							Kalasu				
	FY-1	FY-2	FY-3	FY-4	FY-5	FY-6	FY-7	KLS-1	KLS-2	KLS-3	KLS-4	KLS-5
Li	21.2	22.2	10.7	21.4	23.0	25.3	22.7	57.9	54.7	10.9	52.1	55.8
Be	3.29	1.23	2.52	1.41	0.45	0.71	0.87	3.70	3.56	3.08	5.76	5.60
Sc	3.54	3.62	1.86	1.73	2.91	1.62	1.71	3.40	3.20	6.60	4.90	5.00
V	20.2	19.6	11.4	15.9	19.3	17.5	17.1	15.0	15.0	7.00	22.0	22.0
Cr	4.50	62.3	15.3	10.3	2.37	3.59	2.94	18.0	27.0	11.0	30.0	18.0
Co	2.47	3.42	1.30	2.19	2.45	2.29	1.86	2.40	2.40	1.10	3.00	2.90
Ni	3.20	21.0	5.61	1.71	0.08	14.4	0.04	4.10	4.20	1.20	3.50	3.00
Cu	5.89	8.80	2.82	8.87	3.46	8.05	7.26	4.70	6.00	4.00	3.00	4.80
Zn	26.0	38.3	21.3	27.3	29.0	22.5	25.7	38.0	37.0	27.0	35.0	39.0
Ga	14.0	14.0	13.0	13.3	13.6	11.9	13.5	16.4	15.9	16.9	18.7	19.0
Ge	0.92	0.79	1.05	1.00	1.05	0.74	0.80	0.10	0.11	0.08	0.15	0.16
As	0.84	0.41	0.07	0.28	0.19	0.02	0.13	1.00	1.40	0.50	0.90	1.60
Rb	96.7	97.4	102	100	95.4	96.3	102	236	242	205	226	238
Sr	171	179	141	160	164	163	178	74.1	78.6	34.1	142	141
Y	14.9	15.0	14.0	15.6	15.5	15.0	14.0	18.5	17.9	18.0	38.5	37.7
Zr	141	144	117	125	141	133	125	92.0	91.0	86.0	228	210
Nb	4.66	4.74	4.96	4.81	4.78	4.65	4.97	11.3	10.7	10.4	24.4	24.4
Cs	1.09	1.08	0.89	1.39	0.96	1.30	1.19	16.6	16.0	4.70	15.9	8.73
Ba	648	643	613	607	648	639	673	258	274	284	333	339
La	21.2	20.8	20.6	21.7	21.4	20.2	19.8	18.2	17.2	8.30	32.4	27.5
Ce	43.1	43.3	40.5	41.5	41.9	40.8	39.3	38.7	37.2	31.2	78.2	70.1
Pr	4.36	4.41	4.19	4.54	4.47	4.36	4.10	4.81	4.50	2.41	7.36	6.26
Nd	15.6	15.6	15.3	15.5	16.6	15.2	14.4	18.2	17.0	9.40	25.9	22.4
Sm	3.05	2.91	2.77	2.98	3.18	2.79	2.79	4.25	3.91	2.59	5.34	4.85
Eu	0.50	0.55	0.46	0.52	0.52	0.56	0.51	0.56	0.58	0.22	0.85	0.83
Gd	2.36	2.53	2.42	2.57	2.44	2.61	2.39	3.79	3.62	2.87	5.25	5.08

Tb	0.39	0.40	0.37	0.40	0.39	0.39	0.36	0.65	0.59	0.57	0.91	0.92
Dy	2.29	2.20	2.25	2.44	2.32	2.19	2.06	3.40	3.18	3.63	5.61	5.74
Ho	0.45	0.47	0.47	0.52	0.48	0.47	0.42	0.66	0.62	0.81	1.26	1.27
Er	1.37	1.49	1.46	1.48	1.36	1.35	1.29	1.62	1.56	2.37	3.80	3.86
Tm	0.20	0.20	0.19	0.22	0.20	0.20	0.20	0.25	0.21	0.40	0.58	0.63
Yb	1.47	1.59	1.49	1.53	1.65	1.50	1.52	1.50	1.32	2.96	4.16	4.13
Lu	0.24	0.26	0.23	0.25	0.25	0.23	0.24	0.22	0.22	0.46	0.68	0.66
Hf	3.97	4.14	3.75	4.10	3.99	3.82	3.56	3.00	3.10	4.10	6.30	6.10
Ta	0.50	0.53	0.56	0.51	0.49	0.44	0.51	1.80	2.00	2.00	2.90	2.60
W	0.13	0.31	0.17	0.20	0.34	0.18	0.20	4.00	3.00	1.00	1.00	3.00
Pb	15.1	14.4	17.6	16.3	14.1	15.2	14.3	236	242	205	226	238
Th	9.60	9.80	10.2	9.90	9.45	8.99	9.60	14.5	13.3	14.8	27.5	25.0
U	1.40	1.34	1.63	1.63	1.46	3.11	1.46	2.26	2.20	1.11	5.24	6.92

Table 2 (continued)

Sample	Halasu					Shangkelan								
	HLS-5	3081*	3082*	3083*	3084*	SKL-1	SKL-2	SKL-3	SKL-4	3212^	3214^	3211^	32112	XSK-2^
Li	30.7	43.6	44.3	52.6	256	21.6	15.9	60.3	67.7	-	-	-	-	-
Be	2.22	2.77	2.53	3.02	13.3	9.32	18.1	13.5	8.50	-	-	-	-	-
Sc	5.46	7.31	6.80	7.49	9.8	5.87	7.89	11.3	4.04	-	-	-	-	-
V	16.8	35.2	28.3	22.7	38.3	2.71	2.09	0.11	2.10	-	-	-	-	-
Cr	7.40	9.42	8.11	5.83	6.24	1.95	5.74	3.68	9.06	-	-	-	-	-
Co	2.82	4.88	4.22	3.41	5.35	0.47	0.34	0.19	0.15	-	-	-	-	-
Ni	2.39	20.7	6.31	3.72	4.48	0.03	0.73	0.51	0.77	-	-	-	-	-
Cu	2.64	12.8	3.92	10.4	2.91	1.32	1.62	0.98	1.06	-	-	-	-	-
Zn	48.3	38.2	33.1	40.5	88.6	10.8	15.4	12.5	16.0	-	-	-	-	-
Ga	15.5	18.9	18.1	18.7	23.4	22.9	27.8	28.4	26.6	35.1	37.1	35.1	37.1	33.5
Ge	1.21	-	-	-	-	1.92	2.47	2.56	2.28	-	-	-	-	-
As	0.69	-	-	-	-	0.05	0.07	0.17	0.04	-	-	-	-	-
Rb	135	165	176	181	445	315	293	298	319	390	348	390	348	528
Sr	110	156	122	100	129	15.7	14.3	30.0	24.2	83.6	52.7	83.6	52.7	248
Y	31.2	45.4	39.0	56.2	48.4	31.5	37.9	15.5	35.4	30.9	40.7	30.9	40.7	47.7
Zr	197	-	-	-	-	41.3	47.1	39.7	23.6	168	102	168	102	184
Nb	12.8	13.5	13.7	19.4	30.7	51.4	118	48.8	65.0	59.0	62.0	59.0	62.0	87.1
Cs	6.66	8.54	9.8	11.3	82.8	3.32	3.77	3.91	2.94	-	-	-	-	-
Ba	357	545	412	276	476	24.4	20.2	20.9	41.1	171	152	171	152	193
La	29.9	53.5	41.7	42.5	48.7	13.4	19.7	6.06	13.0	-	-	-	-	-
Ce	62.3	112	87.3	89.0	100	27.2	43.2	10.7	24.9	159	80.3	159	80.3	131
Pr	7.55	13.7	10.8	11.1	12.2	3.49	4.91	1.36	3.05	-	-	-	-	-
Nd	28.0	51.2	41.8	42.6	47.6	12.0	17.1	4.65	10.9	-	-	-	-	-
Sm	5.75	10.3	8.65	8.60	9.13	3.27	3.92	1.31	2.98	10.3	5.49	10.3	5.49	8.64
Eu	1.02	1.36	1.06	1.12	1.90	0.23	0.24	0.17	0.19	1.00	0.58	1.00	0.58	0.69
Gd	5.28	9.45	8.03	8.81	9.7	2.74	3.64	1.22	2.54	6.17	4.25	6.17	4.25	6.30
Tb	0.86	1.56	1.31	1.62	1.62	0.51	0.69	0.26	0.55	-	-	-	-	-
Dy	4.83	9.09	7.76	10.4	9.19	3.69	4.95	1.79	3.91	6.01	6.09	6.01	6.09	5.63
Ho	1.05	1.98	1.63	2.26	2.00	0.77	1.12	0.45	0.88	-	-	-	-	-
Er	2.84	4.90	4.18	6.12	5.32	2.45	3.69	1.53	2.95	-	-	-	-	-
Tm	0.40	0.70	0.60	0.95	0.75	0.45	0.68	0.27	0.55	-	-	-	-	-
Yb	2.80	4.49	3.83	6.34	4.70	4.01	5.69	2.47	5.04	4.56	6.37	4.56	6.37	4.36
Lu	0.43	0.68	0.58	0.97	0.74	0.61	0.99	0.46	0.84	-	-	-	-	-
Hf	4.91	7.49	6.25	7.35	14.6	3.11	3.23	3.12	2.11	-	-	-	-	-
Ta	0.97	1.28	1.40	1.52	2.76	9.11	13.0	5.36	14.5	-	-	-	-	-
W	0.34	-	-	-	-	3.60	7.64	5.55	20.2	-	-	-	-	-
Pb	27.8	34.2	32.3	31.0	32.7	38.8	37.8	35.3	33.3	-	-	-	-	-
Th	13.2	28.9	25.8	20.9	11.2	14.0	27.2	9.5	13.2	-	-	-	-	-
U	1.96	3.23	2.87	5.58	3.58	2.31	7.73	2.66	2.15	-	-	-	-	-

Table 2 (continued)

Sample	Alaer						Xibuodu						
	ALR-1	ALR-2	ALR-3	ALR-4	ALR-5	ALR-6	XBD-1	XBD-2	XBD-3	XBD-4	XBD-5	XBD-6	XBD-7
Li	32.0	30.8	49.6	115	49.4	17.3	10.5	6.85	5.05	8.52	20.0	9.5	12.4
Be	1.22	1.19	2.78	2.94	4.43	5.81	6.03	5.34	2.62	1.99	5.41	5.24	4.21
Sc	4.80	4.80	9.50	8.70	4.20	4.80	1.81	1.72	1.00	0.60	1.10	0.55	0.71
V	28.0	28.0	31.0	30.0	15.0	28.0	0.73	1.61	3.29	0.63	1.59	5.42	4.50
Cr	29.0	20.0	29.0	39.0	47.0	27.0	0.13	1.03	0.20	0.06	10.4	0.59	2.91
Co	3.20	2.90	4.60	4.30	1.80	3.20	0.25	0.40	0.24	0.31	0.55	0.56	0.60
Ni	3.30	2.90	6.90	6.60	4.70	4.20	0.36	1.23	0.45	0.35	15.7	0.56	1.25
Cu	10.8	7.60	2.60	2.20	5.20	7.50	5.68	10.0	18.7	3.87	10.5	2.65	20.4
Zn	25.0	25.0	45.0	54.0	27.0	30.0	12.7	11.0	3.00	8.98	15.6	12.1	12.4
Ga	14.6	14.5	16.4	16.4	20.2	15.0	15.0	13.8	10.6	14.2	16.3	20.5	15.1
Ge	0.12	0.09	0.16	0.15	0.10	0.19	1.02	0.95	0.82	1.19	1.17	1.28	1.06
As	2.00	0.40	0.80	1.00	0.60	0.60	0.20	0.03	0.03	0.17	0.31	0.20	0.27
Rb	95.5	117	145	150	222	144	152	174	149	167	179	187	152
Sr	244	250	173	150	72.5	853	55.1	62.1	59.6	53.0	54.9	32.0	70.2
Y	14.7	15.7	26.6	22.8	15.0	12.3	10.8	7.85	6.04	9.43	8.20	3.54	8.87
Zr	136	132	146	132	85.0	241	37.1	35.2	37.8	35.5	53.9	31.5	49.1
Nb	4.60	4.90	8.10	8.00	11.2	5.70	7.29	7.06	5.26	6.22	8.42	6.19	8.42
Cs	2.46	2.19	12.5	16.6	8.25	8.45	4.81	4.54	3.37	5.08	7.18	3.29	5.19
Ba	637	630	456	352	209	1660	62.3	127	233	64.3	64.2	317	159
La	23.3	22.7	24.4	28.4	21.8	48.6	4.98	4.64	4.05	3.61	2.49	2.71	5.56
Ce	43.6	42.6	50.0	57.7	43.5	88.9	8.74	8.58	6.20	6.96	4.68	2.64	9.9
Pr	4.40	4.31	5.53	6.53	4.93	9.7	1.16	1.02	0.98	0.85	0.57	0.65	1.31
Nd	15.5	15.3	20.4	24.1	17.6	33.4	4.40	3.95	3.61	2.98	2.07	2.15	4.91
Sm	2.99	2.96	4.45	5.20	3.57	5.27	1.14	1.12	0.95	0.93	0.59	0.51	1.24
Eu	0.52	0.50	0.98	1.02	0.54	0.99	0.35	0.34	0.25	0.28	0.34	0.16	0.31
Gd	2.58	2.65	4.35	4.88	3.03	3.68	1.36	1.19	0.92	1.03	0.75	0.47	1.22
Tb	0.38	0.40	0.74	0.75	0.46	0.47	0.24	0.20	0.16	0.19	0.16	0.09	0.22
Dy	2.41	2.61	4.75	4.43	2.82	2.52	1.64	1.33	1.06	1.33	1.15	0.63	1.33
Ho	0.54	0.55	0.97	0.83	0.55	0.46	0.34	0.27	0.21	0.32	0.23	0.12	0.29
Er	1.62	1.60	2.99	2.45	1.45	1.25	1.00	0.79	0.68	0.86	0.83	0.39	0.90
Tm	0.25	0.26	0.45	0.35	0.22	0.17	0.15	0.12	0.10	0.14	0.12	0.06	0.13
Yb	1.60	1.72	2.90	2.39	1.46	1.12	1.10	0.85	0.66	1.04	0.98	0.44	1.04
Lu	0.26	0.27	0.42	0.38	0.22	0.17	0.17	0.14	0.11	0.13	0.16	0.07	0.16
Hf	4.00	4.20	4.30	3.90	2.90	6.20	1.56	1.53	1.70	1.35	2.33	1.60	2.12
Ta	0.40	0.50	0.90	0.80	0.50	2.80	0.90	0.87	0.55	0.77	1.37	0.86	1.06
W	1.00	1.00	1.00	1.00	4.00	1.00	0.55	0.63	0.82	0.17	0.23	1.79	1.02
Pb	113	117	145	150	222	144	29.9	33.3	17.5	31.9	35.1	9.7	36.8
Th	12.2	12.7	11.1	12.4	13.9	14.5	18.3	19.5	20.0	17.3	21.4	16.8	23.7
U	2.17	2.22	2.68	2.38	1.89	1.95	1.10	0.84	0.96	0.99	0.65	0.75	0.97

Notes: Samples marked with * are from Tong (2006). Samples marked with **^** are from Tong et al. (2014a).

Table 3 Sr–Nd–Hf isotopic data for the Chinese Altai granites

Sample	SW-Fuyun					Kalasu	
	FY-1	FY-3	FY-5	FY-6	FY-7	KLS-1	KLS-2
Rb (ppm)	96.7	102	95.4	96.3	102	236	205
Sr (ppm)	171	141	164	163	178	74.1	34.1
$^{87}Rb/^{86}Sr$	1.635944	2.084219	1.683128	1.712992	1.660700	9.215839	17.39565
$^{87}Sr/^{86}Sr$	0.710977	0.712883	0.711086	0.711066	0.710959	0.745548	0.795383
2σ	0.000007	0.000005	0.000005	0.000005	0.000007	0.000008	0.000008
$(^{87}Sr/^{86}Sr)_i$	0.704193	0.704241	0.704107	0.703963	0.704073	0.707927	0.724369
Sm (ppm)	3.05	2.77	3.18	2.79	2.79	4.25	2.59
Nd (ppm)	15.6	15.3	16.6	15.2	14.4	18.2	9.40
$^{147}Sm/^{144}Nd$	0.118047	0.109386	0.115552	0.110505	0.116849	0.141092	0.166478
$^{143}Nd/^{144}Nd$	0.512726	0.512735	0.512733	0.512727	0.512737	0.512344	0.512414
2σ	0.000005	0.000008	0.000007	0.000010	0.000009	0.000010	0.000008
$(^{143}Nd/^{144}Nd)_i$	0.512501	0.512526	0.512513	0.512517	0.512514	0.512079	0.512102
εNd(t)	4.6	5.1	4.9	5.0	4.9	-3.7	-3.3
Lu (ppm)	0.237	0.232	0.249	0.232	0.238	0.220	0.460
Hf (ppm)	3.97	3.75	3.99	3.83	3.56	3.00	4.10
$^{176}Lu/^{177}Hf$	0.008475	0.008800	0.008878	0.008634	0.009480	0.010417	0.015937
$^{176}Hf/^{177}Hf$	0.282996	0.283142	0.283011	0.283036	0.283005	0.282762	0.282807
2σ	0.000006	0.000005	0.000004	0.000006	0.000007	0.000007	0.000005
$(^{176}Hf/^{177}Hf)_i$	0.282950	0.283094	0.282963	0.282989	0.282954	0.282706	0.282721
εHf(t)	0.3	0.0	0.3	0.2	0.3	3.6	4.1
Sample	Kalasu	Halasu				Shangkelan	
	KLS-3	HLS-1	HLS-2	HLS-5	HLS-6	SKL-1	SKL-4
Rb (ppm)	238	135	135	135	135.07	315	319
Sr (ppm)	141	110	110	110	110.48	15.7	24.2
$^{87}Rb/^{86}Sr$	4.901643	3.537694	3.537694	3.537694	3.537694	58.18969	38.14373
$^{87}Sr/^{86}Sr$	0.723791	0.705728	0.717911	0.720206	0.720709	0.872205	0.838043
2σ	0.000006	0.000005	0.000006	0.000005	0.000006	0.000011	0.000013
$(^{87}Sr/^{86}Sr)_i$	0.703781	0.691336	0.703520	0.705814	0.706317	0.699087	0.724564
Sm (ppm)	4.85	5.75	5.75	5.75	5.75	3.27	2.98
Nd (ppm)	22.4	28.0	28.0	28.0	28.0	12.0	10.9
$^{147}Sm/^{144}Nd$	0.130821	0.124216	0.124216	0.124216	0.124216	0.164550	0.165276
$^{143}Nd/^{144}Nd$	0.512584	0.512758	0.512758	0.512758	0.512758	0.512498	0.512719
2σ	0.000007	0.000006	0.000011	0.000008	0.000007	0.000010	0.000007
$(^{143}Nd/^{144}Nd)_i$	0.512338	0.512526	0.512348	0.512350	0.512345	0.512273	0.512493
εNd(t)	1.4	5.0	1.5	1.6	1.5	-0.4	2.3
Lu (ppm)	0.660	0.428	0.428	0.428	0.428	0.607	0.835
Hf (ppm)	6.10	4.91	4.91	4.91	4.91	3.11	2.11
$^{176}Lu/^{177}Hf$	0.015369	0.012363	0.012363	0.012363	0.012363	0.027768	0.056289
$^{176}Hf/^{177}Hf$	0.282934	0.283146	0.282870	0.282894	0.282879	0.282929	0.283073
2σ	0.000004	0.000004	0.000009	0.000007	0.000010	0.000005	0.000005
$(^{176}Hf/^{177}Hf)_i$	0.282852	0.283080	0.282804	0.282828	0.282813	0.282820	0.282853
εHf(t)	8.7	0.0	0.7	0.6	0.7	6.0	7.1

Table 3 (continued)

Sample	Alaer			Xibuodu		
	ALR-1	ALR-4	ALR-6	XBD-3	XBD-5	XBD-7
Rb (ppm)	113	150	144	102	95	102
Sr (ppm)	244	150	444	141	164	178
$^{87}Rb/^{86}Sr$	1.340077	2.893617	0.935212	2.084219	1.683128	1.660700
$^{87}Sr/^{86}Sr$	0.710053	0.723287	0.708919	0.727406	0.736473	0.726478
2σ	0.000007	0.000008	0.000007	0.000008	0.000010	0.000006
$(^{87}Sr/^{86}Sr)_i$	0.705931	0.731777	0.721450	0.721096	0.731377	0.721450
Sm (ppm)	2.99	5.20	5.27	2.77	3.18	2.79
Nd (ppm)	15.5	24.1	33.4	15.3	16.6	14.4
$^{147}Sm/^{144}Nd$	0.116553	0.130368	0.095334	0.109386	0.115552	0.116849
$^{143}Nd/^{144}Nd$	0.512764	0.512345	0.512411	0.512639	0.512623	0.512632
2σ	0.000005	0.000007	0.000004	0.000005	0.000007	0.000006
$(^{143}Nd/^{144}Nd)_i$	0.512599	0.512160	0.512276	0.512486	0.512462	0.512469
εNd(t)	4.7	-3.9	-1.6	2.4	1.9	2.0
Lu (ppm)	0.260	0.380	0.170	0.232	0.249	0.238
Hf (ppm)	4.00	3.90	6.20	3.75	3.99	3.56
$^{176}Lu/^{177}Hf$	0.009233	0.013841	0.003895	0.008800	0.008878	0.009480
$^{176}Hf/^{177}Hf$	0.283031	0.282752	0.282768	0.282871	0.282879	0.282922
2σ	0.000004	0.000005	0.000007	0.000004	0.000005	0.000004
$(^{176}Hf/^{177}Hf)_i$	0.282993	0.282696	0.282752	0.282836	0.282844	0.282858
εHf(t)	12	1.7	3.6	6.5	6.8	7.3

Highlights

- Two episodes of Permian and Triassic high-silica granitoids (HSGs) are recognized in the Chinese Altai.
- Granitoids of both episodes were derived from a mixed source involving juvenile crust and recycled sediment.
- The Permian and Triassic granitoids recorded the tectonic transition from a post-collision to an intraplate setting.
- The post-collision and intraplate tectonism, especially the latter, could facilitate the genesis of HSGs, which drive maturation of continental crust in accretionary orogenic belts.

Graphical abstract